PHASE TRANSITIONS INTO MULTIDOMAIN STATES IN
FERROELECTRIC THIN FILMS WITH DEPLETION CHARGES AND PARTIAL
ELECTRODE SCREENING

by

Hale Nur Çöloğlu

PHASE TRANSITIONS INTO MULTIDOMAIN STATES IN FERROELECTRIC THIN FILMS WITH DEPLETION CHARGES AND PARTIAL ELECTRODE SCREENING

APPROVED BY:

Asst. Prof. Dr. İ. Burç Mısırlıoğlu ....

(Thesis Supervisor)

Assoc. Prof. Dr. Ali Koşar ....

Prof. Dr. Canan Atılgan ....

Asst. Prof. Dr. Gözde İnce ....

Asst. Prof. Dr. Mehmet Yıldız ....

(Co-advisor)

DATE OF APPROVAL: 09.08.2011

PHASE TRANSITIONS INTO MULTIDOMAIN STATES IN FERROELECTRIC THIN FILMS WITH DEPLETION CHARGES AND PARTIAL ELECTRODE SCREENING

Hale Nur Çöloğlu

Materials Science and Engineering, M. Sc. Thesis, 2011

Thesis Supervisor: Assist. Prof. Dr. İ. Burç Mısırlıoğlu

Abstract

This study addresses the limit of ferroelectric functionality for (001) $BaTiO_3$ thin films grown on (001) $SrTiO_3$ substrates sandwiched between pseudomorphic metallic electrodes having perfect and partial screening in the presence of homogeneously distributed ionized impurities for various film thicknesses. The role of thickness, depletion charge density and dead layers on domain formation and phase transition temperatures of ferroelectric films are investigated using the Landau-Ginzburg-Devonshire (LGD) phenomenological approach along with equations of electrostatics and electrostatic boundary conditions. It is well known that dead layers due to finite screening at the ferroelectric-electrode interfaces trigger electrical domain formation. It is demonstrated that depletion charges in the presence of ideal electrodes where polarization charges are fully compensated can also induce a saw-tooth type domain structure. In the presence of dead layers, moderate charge densities result only in a slight tilting of domain walls with respect to the film surface normal while high charge densities stabilize saw-tooth domains. Phase transition temperatures are found to decrease due to depletion charges especially in relatively thick films while this reduction is negligible in thinner films and their phase transition temperatures are nearly the same as charge-free films with dead layers. Comparison with an analytical approach for the phase transition temperature and domain period also supports the results extracted from the numerical approach reported in this thesis. Applied electric field-polarization simulations show that high depletion charges lead to disappearance of the hystereses but this does not necessarily mean disappearance of ferroelectric behavior.

KISMÎ ELEKTROT PERDELEMELİ VE UZAY YÜKÜ İÇEREN FERROELEKTRİK İNCE FİLMLERİN ÇOKLU-DOMEN DURUMUNA DOĞRU FAZ GEÇİŞLERİ

Hale Nur Çöloğlu

Malzeme Bilimi ve Mühendisliği, Yüksek Lisans Tezi, 2011

Tez Danışmanı: Yrd. Doç. Dr. İ. Burç Mısırlıoğlu

Anahtar Kelimeler: Ferroelektrik filmler, geçiş bölgesi yükü, Landau-Ginzburg-Devonshire teorisi, elektrostatik, faz geçişi

ÖZET

Bu çalışma (001) SrTiO$_3$ altlıklar üzerinde büyütülmüş ve psödomorf metal elektrotlar arasına yerleştirilmiş (001) BaTiO$_3$ ince filmlerin farklı kalınlıkları için homojen dağılımlı iyonlaşmış safsızlıkların varlığında ferroelektrik işlevsellik sınırını göstermektedir. Kalınlığın, tükemin yükü yoğunluğunun ve ölü tabakaların ferroelektrik filmlerde domen oluşumunda ve faz geçiş sıcaklıklarındaki rolü Landau-Ginzburg-Devonshire fenomenolojik yaklaşımının elektrostatik denklemler ve sınır koşullarıyla beraber kullanılmasıyla incelendi. Ölü tabakanın ferroelektrik-elektrot arayüzünde sınırlı perdeleme sebebiyle domen oluşumunu tetiklediği bilinmektedir. Polarizasyon yüklerinin tamamen denkleştirildiği ideal elektrotların varlığında, tükenim yüklerinin de testere dişlisi domenleri oluşturduğu gösterildi. Ölü tabakanın varlığında, orta yük yoğunlukları domen duvarlarının yüzey normaline göre az miktarda açılanmasıyla sonuçlanırken yüksek yük yoğunlukları testere dişlisi domenleri kararlılaştırdı. Faz geçiş sıcaklıklarının özellikle görece kalın filmlerde yük yoğunluklarıyla düştüğü gözlemlendi. Daha ince filmlerdeyse bu düşüşün ihmal edilebilecek kadar az olduğu ve daha ince filmlerin ölü tabakalı yüksüz filmlerle aynı faz geçiş sıcaklıklarına sahip oldukları görüldü. Faz geçiş sıcaklığı ve domen periyodunun analitik yaklaşımla çözümü ile karşılaştırması bu çalışmada elde edilen nümerik sonuçları destekledi. Elektrik alan-polarizasyon simülasyonları yüksek yük yoğunluklarının histerezisin yok olmasına yol açtığını gösterdi ancak bu, ferroelektrik fazının yok olduğu anlamına gelmemektedir.

ACKNOWLEDGEMENTS

TABLE OF CONTENTS

LIST OF TABLES

LIST OF FIGURES

LIST OF SYMBOLS AND ABBREVIATIONS

FE : ferroelectric

P_i : polarization components

E_i : electric field components

D_i : dielectric displacement components

E : energy level

LGD : Landau-Ginzburg-Devonshire

T_C : Curie temperature

G_{ij} : gradient energy components

F : free energy

BT : Barium Titanate

ST : Strontium Titanate

RT : Room temperature, 25 °C

S_{ij} : elastic compliance factors

Q_{ij} : electrostrictive coefficients

u_m : misfit strain

α_{ijk} : dielectric stiffness coefficients

Φ : work function

σ_i : stress components

ϕ : potential

ρ : charge density

ε_0 : permittivity of vacuum

ε_i : relative permittivity

CHAPTER 1

INTRODUCTION: FERROELECTRICS

1.1 Crystal Structure and Polarization

Ferroelectrics are a special type of dielectric crystals which exhibit spontaneous polarization in the absence of external electric field. Most of the ferroelectrics are oxides crystallizing in the cubic or pseudocubic perovskite structure with the ABO_3 formula. In this structure A and B are cations that can attain a range of valences between 2+ and 4+ and O is the O^{2-} anion. Covalencies must also be considered in this structure, leading to corrections in the charges of these ions as effective values. A atoms are situated at each corner of the cube, smaller B atom fits in the body center and 6 of O atoms are sharing 6 face centers of the cube, coordinating a octahedra around B. Typical cubic perovskite structure is demonstrated in Figure 1.1.
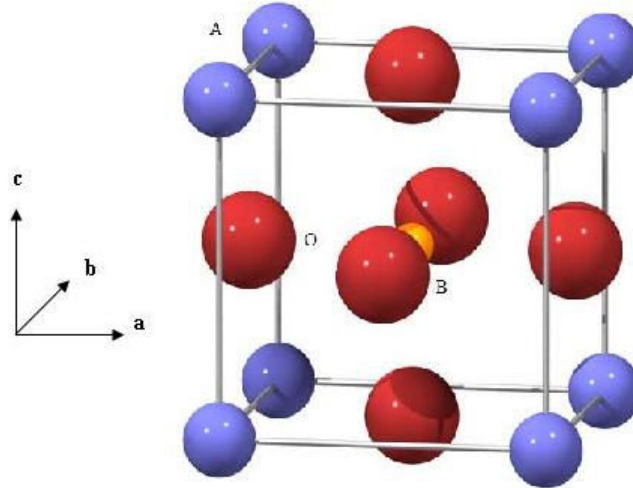
Figure 1.1. Typical perovskite unit cell. Small B cation at the centre, surrounded by O^{2-} octahedra. Large A cations occupy corners of the cube. Axis notations (a,b,c) are shown as well.

Above a critical temperature, namely the transition temperature or the Curie point, that is characteristic for each perovskite ferroelectric material, the crystal has a cubic geometry, and a high symmetry with respect to the central B-site (centrosymmetric) and thus the system is in the paraelectric state. When the material is cooled below the Curie temperature, cubic perovskite transforms into one of non-centrosymmetric lattice structures as shown in Figure 1.2, hence a reduction in crystal symmetry appears. Here reduction in crystal symmetry means that at least one symmetry operation (or element) that was possible in one of the phases is lost. Good examples to ferroelectric transitions in perovskites are $BaTiO_3$ and $PbTiO_3$. $BaTiO_3$ and $PbTiO_3$, transform from cubic to tetragonal at 130 °C and 493 °C, respectively accompanied by the appearance of a spontaneous dipole in each unit cell.

2

$$\text{Tetragonal} \quad P_1 = P_2 = 0 \quad P_3 \neq 0$$
$$\text{Orthorhombic} \quad P_2 = 0 \quad P_1 = P_3 \neq 0$$
$$\text{Rhombohedral} \quad \quad P_1 = P_2 = P_3 \neq 0$$
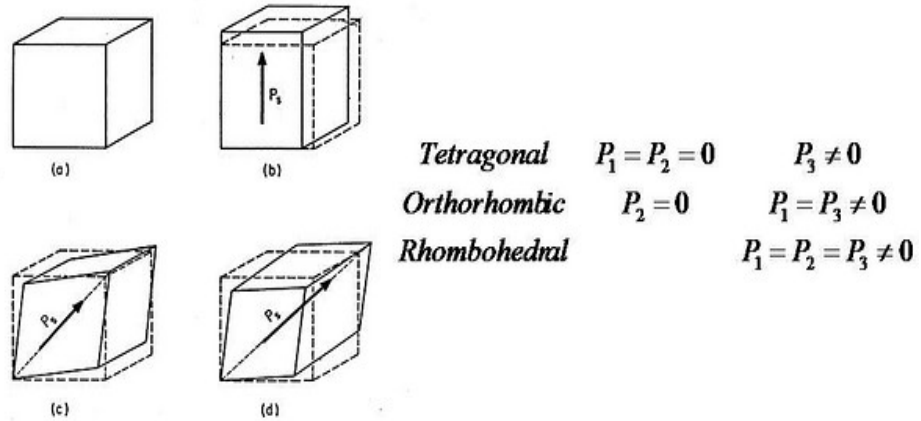
Figure 1.2. The perovskite structure ABO_3, in a) cubic, b) tetragonal, c) orthorhombic, d) rhombohedral symmetry. a) Cubic crystal does not have spontaneous polarization. b) Tetragonal crystal has polarization on z-axis. c) Orthorhombic crystal has polarization on the direction of combination of z- and x-axes. d) Rhombohedral crystal shows polarization on the direction of combination of all principal normal axes.

BaTiO$_3$, however, is not stable in tetragonal form at lower temperatures, it has two more phase transitions; at 5 °C tetragonal to orthorhombic, at -90 °C orthorhombic to rhombohedral [1]. Cohen states that the covalent hybridization between B cation and O weakens short range B-O repulsion while A hybridization with O states leads to larger strain which favours ferroelectric distortions and also indirectly affecting B-O interactions. In these cases the spontaneous polarization emerges, that is the basis of ferroelectric behaviour, by collective displacement of the central atom of the each unit cell relative to anions, creating a self-induced dipole moment. These dipoles interact with each other such that the interaction produces an internal field which eventually lines up the dipoles and saturates the spontaneous polarization. During the structural shifts, the crystal elongates in c-direction and c/a ratio of the unit cell deviates from unity, which is another way of tracking the phase transformation in ferroelectrics [2].

3

1.2 Crystal Symmetry

In nature, there exist 230 space groups of crystal symmetry in 3 dimensions governed by 14 Bravais unit cell structures which belongs to one of seven crystal lattice systems and 32 point groups in Table 1 which consist of symmetry operations that keep the pattern of symmetry unmodified.

Table 1.1. Point groups for seven crystal systems

Crystal Structure	Point Groups	Centrosymmetric	Non-centrosymmetric	
			Piezoelectric	Pyroelectric
Triclinic	1,1	1	1	1
Monoclinic	2, m, 2/m	2/m	2, m	2, m
Orthorhombic	222, mm2, mmm	mmm	222,mm2	mm2
Tetragonal	4, 4, 4/m, 422, 4mm, 42m, (4/m)mm	4/m, (4/m)mm	4, 4, 422, 4mm, 42m	4, 4mm
Trigonal	3, 3, 32, 3m, 3m	3, 3m	3, 32, 3m	3, 3m
Hexagonal	6, 6, 6/m, 622, 6mm, 6m2, (6/m)mm	6/m, (6/m)mm	6, 6, 622, 6mm, 6m2	6, 6mm
Cubic	23, m3, 432, 43m, m3m	m3, m3m	23, 43m	

These operations are rotation (which can only be 1-, 2-, 3-, 4- and 6- fold), inversion (again can only be 1-, 2-, 3-, 4- and 6- fold), reflection (can be horizontal, vertical or

diagonal mirror planes to the rotation axes), translation (which does not fix a point), screw and glide which are actually a combination of rotation or reflection with translation, respectively. Of the thirty-two point groups, eleven groups have a center of symmetry, so they do not polarize. A crystal having no center of symmetry possesses at least one crystallographically unique directional axis. All non-centrosymmetric point groups, except the 432, have piezoelectricity along unique directional axes [3]. Of the twenty piezoelectric point groups, ten (1, 2, m, mm2, 4, 4mm, 3, 3m, 6, and 6mm) have only one unique direction axis which are called polar due to spontaneous polarization.

The polar crystals are also referred as pyroelectric due to the variation of polarization, the dipole moment per unit volume, with respect to temperature. Pyroelectric coefficient is determined as the slope of the polarization versus temperature line in the ferroelectric section. Figure 1.3 is an example of the polarization decrease during heating for $BaTiO_3$, as can be seen from this figure, the polarization immediately goes to zero at Curie temperature.
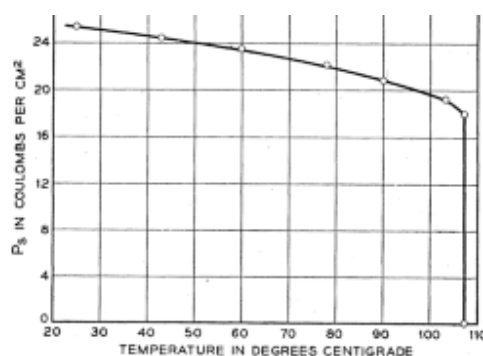
Figure 1.3. Spontaneous polarization versus temperature for $BaTiO_3$. Polarization falls to zero at phase transition [4].

1.3 Hysteresis Loop

The magnitude and direction of spontaneous polarizarion may vary depending on temperature, geometry, stress and type of material. Above Curie temperature, the spontaneity of polarization disappears and ferroelectric transforms into a paraelectric, usually a high dielectric constant (high-k) material when not too far from the Curie point. In

the absence of an external electric field, a macroscopic crystal of ferroelectric with free, non-electroded surfaces, will exist in a state where anti-parallel oriented polarized domains (clusters of parallel aligned dipoles) are present (Figure 1.4). Their total polarization sums to zero in order to satisfy electrostatic neutrality. By the time the external field is applied, the domains of anti-parallel polarization start to align parallel to the field, creating a total nonzero polarization inside the crystal. As the electric field is increased, more anti-parallel domains align parallel to the field. Eventually the whole crystal polarizes in the same direction, where the polarization saturates to its maximum (P_S). After saturation; unlike paraelectrics, which polarize linearly with electric field, (See Figure 1.5), the parallel dipoles do not relax back to original anti-parallel states with the removal of external field: They can remain in an all parallel configuration for some indefinite amount of time in the presence of free surfaces (See Figure 1.4). As, for some time, they prefer to be in the polarized state at zero electric field (Remanent polarization, P_R) and a negative field is required to to switch total polarization in the reverse direction. The field where this happens is called as the coercive field, E_C. Therefore, ferroelectrics are similar to ferromagnetics in the sense of hysteretic behaviour (See Figure 1.6).
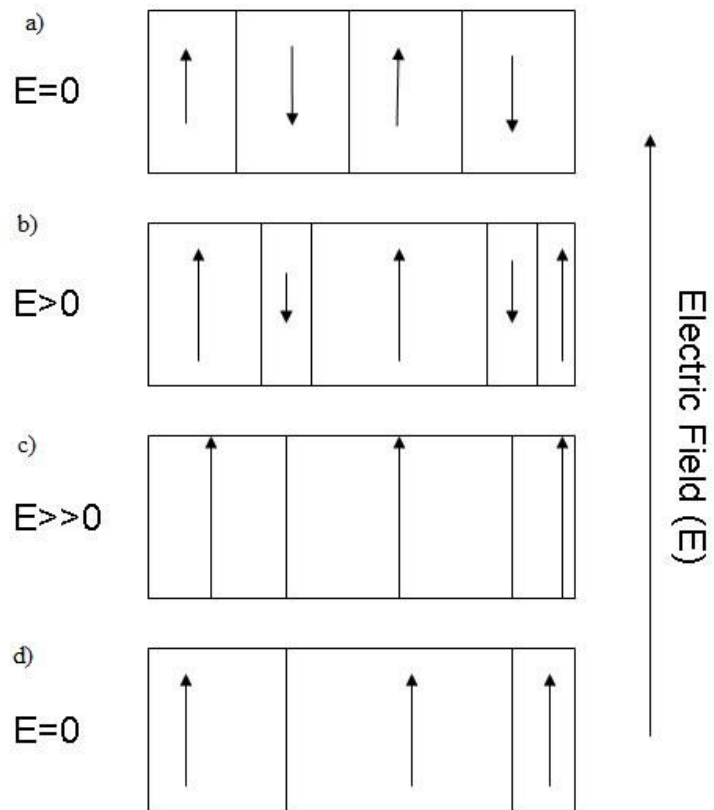
Figure 1.4. Alignment of dipoles in ferroelectric phase. a) Antiparallel alignment, namely domains with no application of electric field. b) Growing of domains in existence of the electric field in the same direction. c) Application of higher electric field: All crystal polarized parallel to the field. d) Removal of field, dipoles forming the "remnant polarization" state.
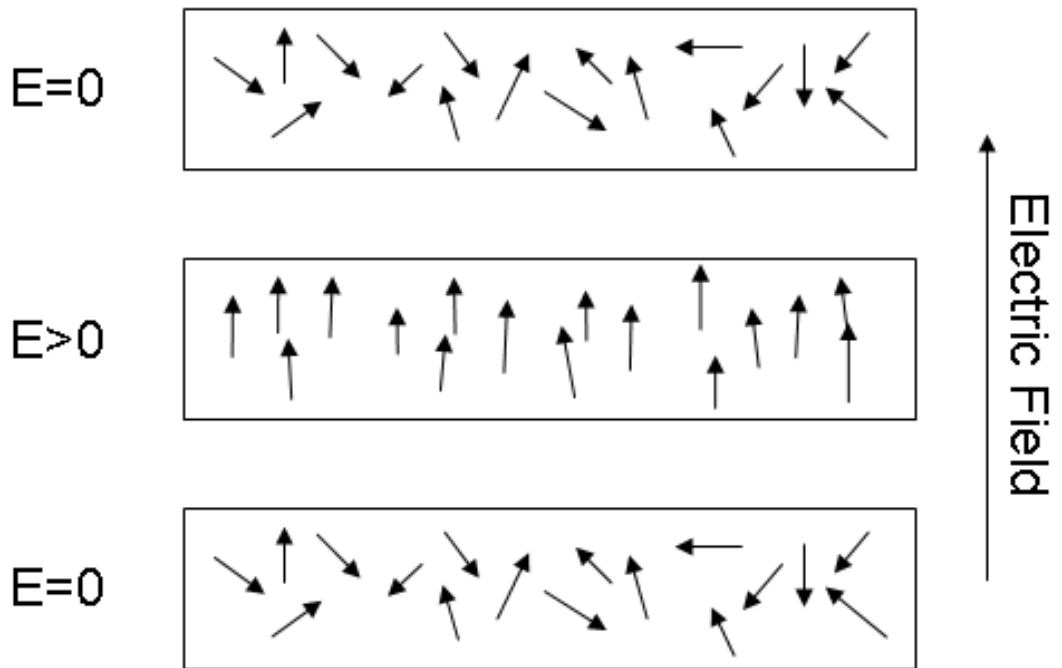
Figure 1.5. Alignment of dipoles in paraelectric phase. a) No alignment with no application of electric field. b) Growing of "up" aligment in existence of the electric field. c) Relaxation of "up" aligned dipoles with removal of electric field.
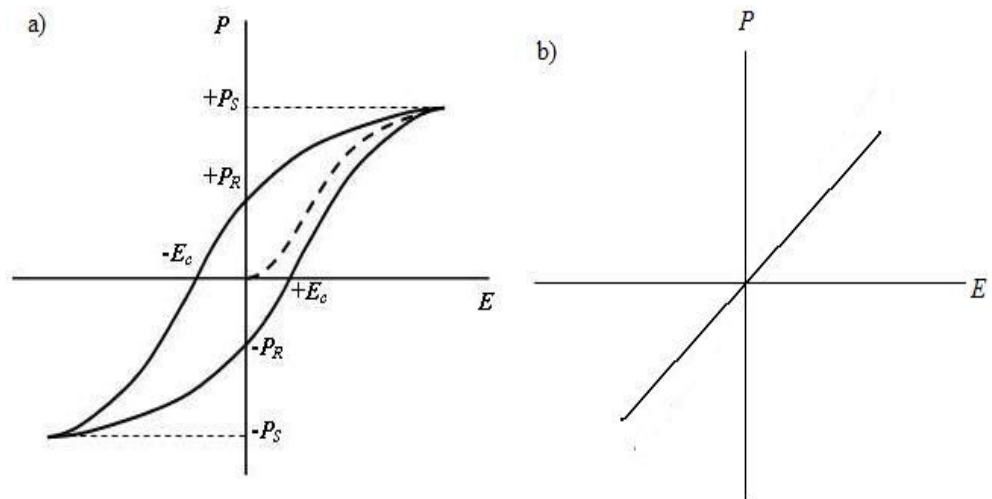
Figure 1.6. Hysteresis loops of a) ferroelectric with spontaneous and remanent polarization and b) paraelectric phase ($T > T_C$) with linear relation between polarization and external field.

1.4 Domain Formation

With the emergence of spontaneous polarization at transition temperature, the surface of ferroelectric is populated by bound charges of polarization. This surface charge produces an electric field, called depolarizing field due to its opposite orientation to the spontaneous polarization (See Figure 1.7a). The depolarizing field will form whenever there is a nonhomogeneous distribution of spontaneous polarization, for example, due to the fall-off of the polarization near the free surface of a ferroelectric (polarization is zero outside the ferroelectric and nonzero inside) [5]. The depolarizing field can be so strong that it can destroy the stability of single domain ferroelectric state and can lead to domain formation in opposite orientations in order to minimize the electrostatic energy related to it [6]. An alternative solution to the minimization problem of the depolarizing field is compensation by free charges from a surrounding material, namely an ideal metal electrode (Figure 1.7b). However, in real life, electrodes deviate from ideal behaviour and often they can not completely compensate for depolarizing field. Thus ferroelectric domains with domain widths form depending on the competing strengths of depolarizing field and spontaneous polarization. (Figure 1.7c).
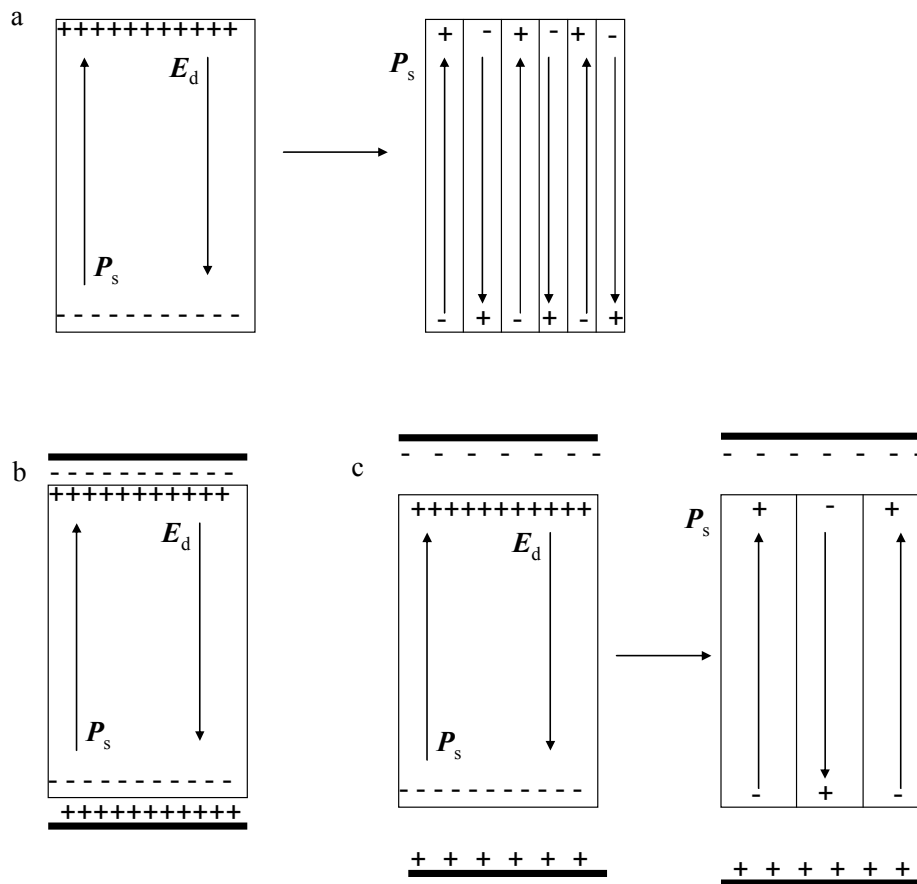
Figure 1.7. a) A free standing ferroelectric, surface is exposed to air, domain splitting due to depolarizing field b) Total compensation of bound charges by ideal electrode charges c) Partial compensation of bound charges by non-ideal electrode charges, a finite screening length at the metal surface which will be mentioned in section 2.1.2.

1.5 Applications

The main application for ferroelectrics has been to incorporate them as functional components into microelectronic devices, by tailoring spontaneous polarization states as memory. In addition to application potential in memories, these materials also have dielectric tunability (dielectric constant is a function of the externally applied field), a strong piezo response and recently investigated electrocaloric and infrared properties. Early use of ferroelectrics start with capacitors and piezoelectric transducers and actuators. The

10

widespread use of $BaTiO_3$ in 1950s is followed by $PbTiO_3$, lead zirconium titanate (PZT), lead lanthanum zirconate titanate (PLZT) and lead magnesium niobate ($Pb(Mg_{0.33}Nb_{0.66})O_3$, PMN) for a variety of applications from medical ultrasound imaging to aerospace technologies. With recent devolopments of thin film and ceramic processing technology ferroelectric thin films are considered for non-volatile ferroelectric memories (FRAMs), Dynamic Random Access Memories (DRAMs), Micro-Electro-Mechanical Systems (MEMS), tunable devices, micro-armours and infrared sensors. For a ferroelectric material to be successful in application, it should have a low coercive field, high remanent polarization, long cycle durability, suitable mechanical strength and negligible deviation in chemical composition. Complex perovskite compositions such as $BaTi_{0.91}(Hf_{0.5}Zr_{0.5})_{0.09}O_3$ (BTHZ-9) have been strong candidates for thin film devices since solid solutions enable the tuning of the physical properties in a beneficial way. [5, 7, 8]

CHAPTER 2

THIN FILM FERROELECTRICS

2.1. Bulk versus Thin Film

Compared to the bulk forms, thin film ferroelectrics can have significantly inferior electronic properties in terms of capacitance, permittivity and remanent polarization as well as a reduced Curie point depending on the thickness of the film, type of the substrate, lattice mismatch between the film and substrate, concentration of defects and effect of electrostatic boundary conditions of the film. Another aspect well understood in these systems is that ferroelectrics behave as wide bandgap semiconductors. This behaviour, of course, leads to several consequences. For instance, impurities in a ferroelectric film are nearly inevitable owing to growth and processing conditions. These impurities behave as dopants in similar lines to the case of doped semiconductors and a depletion region in the ferroelectric film might form. Therefore it is quite instructive to revise the general characteristics of a metal-semiconductor junction before proceeding to the case of depletion charges in ferroelectric films.

2.1.1. Metal – Semiconductor Junctions

The performance of a capacitor device is heavily dependent on the quality of the interface between the ferroelectric/electrode and electrode/substrate heterostructure [9]. Therefore it is vital to understand the details of metal-semiconductor interfaces since ferroelectrics are often considered as wide bandgap semiconductors. Good examples are $BaTiO_3$ and lead–lanthanum–zirconate–titanate (PLZT), having a bandgap of around 3 to 4 eV. A region of depletion charges, for instance in the case of a Schottky contact, is expected to create internal electric fields which, in the case of a polarizable medium such as a ferroelectric, can significantly impact the electrical characteristics. In addition, it should be kept in mind that due to this fact, the electric field will also not be constant over the ferroelectric film volume [10]. It must also be kept in mind that the interface, can have an Ohmic character. In this thesis, we will keep our focus on the Schottky type interfaces as this is often reported to occur in ferroelectric thin films [11]. A comparison of the Schottky and Ohmic contact is given in Figure 2.1 for reference. A summary of the formation of a Schottky and an Ohmic interface is provided in the upcoming sections.
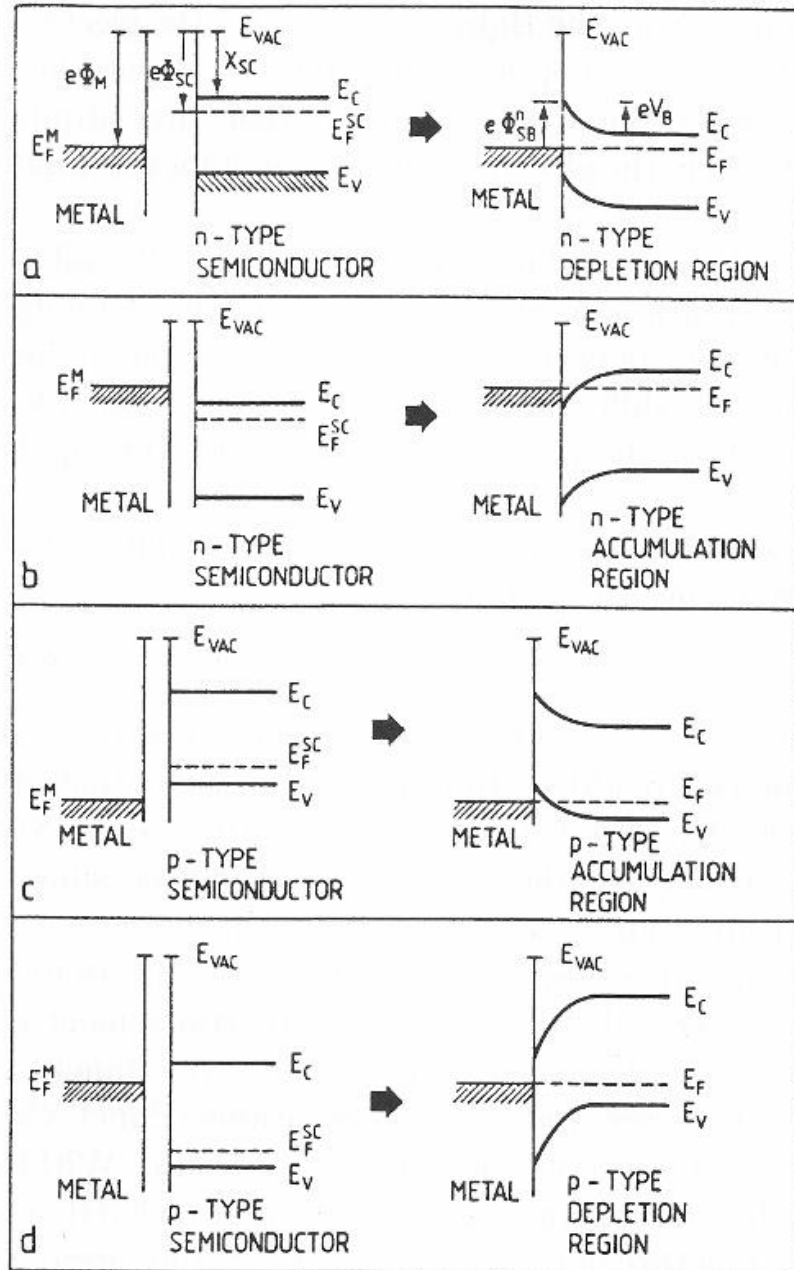
Figure 2.1. Metal-semicoductor junctions. a) High-work-function metal and n-type semiconductor, Schottky b) Low-work-function metal and n-type semiconductor, Ohmic c) High-work-function metal and p-type semiconductor,Ohmic d) Low-work-function metal and n-type semiconductor,Schottky. The energy of the bands is plotted as a function of distance z in a direction normal to the surface. E_{VAC}, vacuum energy; E_C, energy of conduction band minumum; E_V, energy of valence band maximum; E_F, Fermi level energy [12].

14

2.1.1.1 Schottky contact

When a metal is brought into contact with a semiconductor, two scenarios are possible depending on the material type. Initially, the two materials will attain the same Fermi level since the chemical potential has to be uniform throughout the system at equilibrium [13]. The level of the work function (Φ) of the metal, which is the energy difference required to excite an electron from its chemical potential (E_F) to the vacuum (E_{VAC}) with zero energy, with respect to the dopant levels in the semiconductor determines the direction of the flow of charge carriers in order to equate Fermi levels. Electrons flow from low work function material to the high work function one, in this way they also guarantee to lower their energy level. For the Schottky contact case of a metal/n-type semiconductor, where Φ_s is lower than Φ_m (See Figure 2.1a), the surface electrons of semiconductor tend to flow to the metal surface. The flow continues until metal surface becomes negatively charged enough so as to equate the Fermi levels, resulting in a region near the semiconductor-electrode interface that is depleted of negative carriers, hence a positively charged impurity zone is formed. This situation causes the bending of semiconductor energy bands, lowering them with respect to the levels before the junction was made. As seen from Figure 2.1 even the band bending is inevitable, the band gap remains constant as well as the position of the band edges away from the interface. Due to the accumulation of electrons on the side of the metal, there is a positively charged region in the semiconductor as aforementioned and it is called the depletion zone. The approximately spatially uniform ionized donors are assumed to be the only source of charge in this region. Depletion zone creates a built in potential between positively charged semiconductor side and negatively charged metal side and due to the energy barrier (Schottky barrier, ϕ_B) between metal and depletion zone, this type of contact is also called as 'blocking contact'.

It is important to understand the width of this depletion zone as it behaves like a capacitor. An approximate but effective and widely accepted way to find the width of this zone is as follows: The potential of the Schottky barrier can be derived with some boundary

15

conditions which are zero electric field ($E_1 = -\partial\phi / \partial x = 0$) and Schottky barrier potential ($\phi = \phi_B$) at depletion layer width (x=w_d) as well as zero potential ($\phi = 0$) at the interface (x=0). Accordingly, the Schottky barrier potential, ϕ_B is expresses as [14]

$$\phi_B = \left(\frac{\rho}{2\varepsilon_r\varepsilon_0} \right) w_d^2, \tag{2.1}$$

where ρ is charge density, ε_r is relative permittivity and ε_0 is the permittivity of vacuum. From Eq. (2.1), the dependence of width of depletion layer and charge density on Schottky barrier is clear.

If the semiconductor is p-type, Schottky contact will be formed when Φ_s is higher than Φ_m (See Figure 2.1d). In this case electrons will flow from the metal to the semiconductor, so the depletion zone will have excess of electrons and hence negatively charged. Apart from these differences, the behaviour of the contact in case of an externally applied voltage will be the same: Forward bias will reduce the depletion width and reverse bias will increase. Note that terminal connections will be reversed for p-type and n-type semiconductor, i.e., when n-type semiconductor is connected to negative end, it creates a forward bias while p-type semiconductor creates a reverse bias when connected to negative end.

2.1.1.2. Ohmic contact

On the other hand, in Figure 2.1b, another metal – n-type semiconductor junction, where Φs is higher than Φ_m, is shown. In this case metal donates electron to semiconductor, enriches the region with negative charge carriers, while itself becoming slightly positive with the positive charges of the remainings of flowed electrons. Therefore the region becomes an 'accumulation layer' (Ohmic contact) where the carriers are free to flow in or out of the semiconductor so that there is a minimal resistance across the contact [15].

Two opposite forces establish the balance of accumulation layer in the absence of external electric field. First, a pull toward the metal since the electrons in the accumulation layer are in a region with an electric field and metal consists the positive end of this field.

Second, a diffusion force toward the semiconductor since the electron density in accumulation layer is higher than the rest of the semiconductor. A steady state condition is satisfied by equilibrium of these forces.

It is worth mentioning that far from the interface the band structure of semiconductor remains unchanged except for the overall energy decrease even the surface bands can be said to pinned to metal bands.

2.1.2 Interfacial Capacitance

Within the depletion layer the packing of the atomic layers might differentiate which leads to modifications in electrical properties. Therefore there is always an interface which experimentally exhibits a different capacitance property. The electric field penetrates into the electrode over a very short screening interface and this screening layer manifests itself as some additional interfacial capacitance [16]. In a very general sense, the experimental capacitance of thin films fits into the empirical relation [17]:

$$\frac{1}{c} = \frac{1}{c_i} + \frac{t}{\varepsilon_f} \tag{2.2}$$

Here c is the capacitance per unit film area and t is the film thickness; c_i anf ε_f are interpreted as the interfacial capacitance and the film permittivity, respectively. At a ferroelectric/metal electrode interface, depletion region leads to formation of a interfacial ferroelectrically "dead" layer with substantially lower permittivity. The consequences of the so called dead layer cover both reduction in transition temperature and amplified thickness dependence of ferroelectricity as well as fatigue [18]. Interfacial capacitance can be quite detrimental especially in ultrathin films. In thermodynamic analysis of ferroelectric thin films, relation given in Eqn. 2.2 is ultimately not sufficient to explain the results and the mechanisms with which the aforementioned degradation occurs. In the work carried out in this thesis dead layers will be introduced to justify the effects of such formations on the phase transition temperature and domain characteristics of ferroelectric thin films.

2.2. Residual Stresses

The formation of defects such as ionic vacancies, interstitials and dislocation networks are inevitable owing to both the process conditions and the developing strains in the film on misfitting substrates during fabrication. An additional cause of permittivity reduction in thin films is the residual stresses caused by these defects. The discrepancy between lattice constants of substrate and film, measured as misfit strain; $u_m=(a_{subs}-a_{film})/a_{subs}$, originates either from tensile or compressive stresses on the film. Apart from misfit strain, there exist the self-strain of the film on substrate, due to the change of a lattice parameter during phase transition from cubic to tetragonal crystal structure. The stress in the plane of the film causes a change in permittivity according to the following relation [17]

$$\frac{1}{\varepsilon_f} = \frac{1}{\varepsilon_u} - 4Q_{12}\sigma \,, \tag{2.3}$$

where ε_f is the permittivity of stressed film, ε_u is the permittivity of unstressed, free-standing film, Q_{12} is the electrostrictive coefficient and σ is the stress due to the misfit. Electrostrictive coefficients and their contribution to free energy of the films will be further discussed.

The residual stresses, apart from their direct effect on permittivity, also lead to dislocations at the substrate-film interface where the interfacial misfit strain is relaxed by formation of edge type misfit dislocations [19]. It has been shown that these dislocations lead to polarization gradients across the interfaces which enhances depolarization fields and degrades ferroelectricity by pinning domain switching [20, 21]. However, details of the stress effects are not in the scope of this thesis, therefore they will not be further discussed in the forthcoming chapters.

2.3. Presence of Depletion Charge in Ferroelectric Thin Films

Other than the dislocations, point defects are a significant part of challenges against the control of ferroelectricity in thin films. Vacancies, especially oxygen vacancies, have long been known to be the dominant type of point defects in perovskite oxides [22, 23]. Several experimental conditions such as oxidation processes and donor dopants have been adopted to eliminate oxygen vacancies; however they could only minimize the density of vacancies. The major impact of these charged defects is their contribution to the formation of depletion zone in the metal-ferroelectric interface. Hence, ionized impurities are usual consequences of an interface between a metal and a ferroelectric. The studies of diffusive properties of charged defects reveal that near room temperature charged defects are nearly immobile and might get populated at interfaces and defect sites after several thousands of applied field cycles [24]. Nevertheless, how the evolution of these charges under limited lattice diffusivities will be impacted by size effects remains to be understood as an important aspect.

In a real ultrathin ferroelectric film with a few tens of nanometers maximum, the electrostatic conditions have to be adjusted at very short distances like a few unit cell thicknesses. Therefore huge potential gradients are imperative, increasing both the importance of the interaction between depletion charges and the screening at the film-electrode interface. As the film thickness is comparable or smaller than the depletion zone width of a ferroelectric in contact with electrodes and if the film has typical densities of impurities, the entire ultrathin film can be said to be depleted, meaning that the ionized impurities are homogeneously distributed. Depletion widths of around 30 nm and ionized impurity densities of around $10^{23-27}/m^3$ have been reported by Pintilie *et al.* using interfacial capacitance measurements for $PbZr_{0.2}Ti_{0.8}O_3$ films [25, 26].

The attempts to clarify the effects of depletion charges have been confined to very simple charge distribution models because analytical solutions of system with realistic charge distribution models make the problem more formidable. The few studies that deal with the effect of continuous charge distributions have only considered the single domain states[27, 28]. However, even the homogeneous charge distribution may significantly alter

the potential map, increasing the inhomogeneity throughout the film. Then, multidomain configurations at phase transition to ferroelectric state as well as discrepancies at calculated transition temperatures can become possible. Bratkovsky and Levanyuk [29] have analytically attempted the problem of depletion charges in ferroelectric thin films by considering several charge distributions. They clearly discussed suppression of ferroelectricity in the near electrode region due to the built-in polarization and splitting into domains at low temperatures for small size systems where screening of the impurity charge becomes ineffective and depletion effect becomes pronounced [29]. On the other hand, their study assumed the electrodes as ideal and the consequences derived for systems with ideal electrodes will have to be modified for non-ideal, real electrode systems where dead layer comes into play.

CHAPTER 3

THEORY AND METHODOLOGY

3.1. General Concepts of Landau Theory for Ferroelectrics

A powerful approach to deal with phase transitions is to use phenomenological theories, which simply describe the phenomena on a macroscopic scale neglecting individual contributions from the atoms, namely using continuum medium approximations. In 1937, Landau first described second order phase transitions, where he chose an order parameter in the system to describe the general characteristics of the transition for many types of systems. This successful approach was extended to first order transitions in ferroelectric crystals by Devonshire in 1949. As to deal with polarization fluctuations, with the contributions of Ginzburg, the theory is later on was named as the Landau-Ginzburg-Devonshire (LGD) Theory [30]. In this methodology proposed by Landau, an internal variable or some degree of freedom of the system is sought corresponding to the order parameter that is zero in one phase and non-zero in the other phase, where the latter is usually called the "lower symmetry phase" in crystals. A good example to this is magnetization of ferromagnetic crystals, where in the paramagnetic phase the spins are disordered so that total magnetization is zero while in ferromagnetic phase, spins are parallel-aligned and total magnetization is nonzero [31]. For ferroelectrics, the order

parameter is spontaneous polarization, P, which emerges in ferroelectric phase with parallel alignment of electric dipoles and disappears in the paraelectric phase. After the order parameter is determined, the equations of state is defined from the free energy (F) that suffices to represent both phases as a function of temperature (T) and order parameter ($\mathbf{P}$). The equilibrium of an isothermal system is the minimum of the free energy with respect to the order parameter; $\partial F(T,P)/\partial P = 0$. Landau expanded the free energy density function with respect to the order parameter into a power series [30]

$$F(T,P) = F_0(T) + \alpha_1 P^2 + \alpha_{11} P^4 + \alpha_{111} P^6 - EP , \qquad (3.1)$$

where $\alpha_1 = (T - T_C)/2\varepsilon_0 C_0$. T, T_C and C_0 are temperature, Curie temperature and Curie constant, respectively. α_{11} and α_{111} are higher order dielectric stiffness constants [27, 32]. F_0 is not a function of order parameter, it is the energy due to enthalpy and entropy, so it also stands for the energy of the paraelectric phase. The coefficients of order parameter are dielectric stiffness coefficients relating polarization to the electric field. When $E = 0$, the solution of the polarization from minimization of the free energy in Eq. (3.1) with respect to P yields

$$P^2(T) = \frac{-\alpha_{11} + \sqrt{\alpha_{11}^2 - 3\alpha_1\alpha_{111}}}{3\alpha_{111}} \qquad (3.2)$$

Another quantity that can be derived from Eq. (3.1) is dielectric permittivity. When electric field is nonzero but small

$$\frac{dF}{dP} = E = 2\alpha_1 P + 4\alpha_{11} P^3 + 6\alpha_{111} P^5 \qquad (3.3)$$

Since $P/E = \varepsilon_0\chi$, and susceptibility is $\chi = \varepsilon_r - 1$, dielectric permittivity of a ferroelectric can be calculated as $\varepsilon = \varepsilon_0(1 + 1/(2\alpha_1 + 4\alpha_{11} + 6\alpha_{111}))$. However, this relation is only useful under small electric fields where hysteretic behaviour has not dominated yet. Also, Eq.(3.3) cannot be used to extract or predict the hysteresis behaviour of the ferroelectric crystal since it only handles polarization switching from a thermodynamic instability approach, whereas in hysteresis behaviour, metastable phases emerge and exist among several temperature and field ranges.

According to Eq. (3.2), different orientations of the same phase in equilibrium may coexist. Then there might be a domain structure and domain walls where order parameter changes its sign. In order to include the domain wall energy to the system, gradient terms of order parameter have to be incorporated into the equation. For an isotropic system with unidirectional polarization, Ginzburg-Landau Equation is [30, 33]

$$F(T,P) = F_0(T) + \alpha_1 P^2 + \alpha_{11} P^4 + \alpha_{111} P^6 + G(\nabla P)^2 - EP \qquad (3.4)$$

The general assumption is that G is a positive coefficient meaning that domain wall costs extra energy to the system. Gradient energy becomes more important for thin layers, where inhomogeneity in polarization is relatively denser for the whole system.

3.2. Modification of the Landau Theory for Ferroelectric Thin Films

As mentioned in the previous chapter, there are stresses on thin films due to the clamping to the substrate. These stresses couple to the polarization through the electrostrictive effect and can significantly alter the bulk characteristics [34]. Also, due to the anisotropy in geometry, i.e., two dimensions are subjected to the substrate while the third axis is free, three directions of polarization should be considered separately and cross terms between them should also be taken into account. In this section, the thermodynamic Landau free energy contributions to the ferroelectric thin film system clamped on a misfitting substrate will be given in the single domain homogeneous polarization state. The total energy can be written as

$$F_{total} = F_{polarization,P} + F_{elastic,E} + F_{electrostatic,ELECTRO} \qquad (3.5)$$

The energy due to the polarization in three dimensions is the first and major contribution:

$$\begin{aligned}
F_P = {} & \alpha_1(P_1^2 + P_2^2 + P_3^2) + \alpha_{11}(P_1^4 + P_2^4 + P_3^4) + \alpha_{12}(P_1^2 P_2^2 + P_1^2 P_3^2 + P_2^2 P_3^2) \\
& + \alpha_{111}(P_1^6 + P_2^6 + P_3^6) + \alpha_{112}[P_1^4(P_2^2 + P_3^2) + P_2^4(P_1^2 + P_3^2) + P_3^4(P_1^2 + P_2^2)] \quad (3.6) \\
& + \alpha_{123}P_1^2 P_2^2 P_3^2
\end{aligned}$$

where all α are dielectric stiffness coefficients. It is worth mentioning that Voigt matrix

notation and rectangular Cartesian frame of reference with x_3 (z-) axis perpendicular to film-substrate interface are used throughout the study. Internal elastic energy due to strain is the second major contribution in a thin film:

$$F_E = \frac{1}{2} C_{ijkl} \left(u_{ij} - \varepsilon_{ij}^0 \right)\left(u_{kl} - \varepsilon_{kl}^0 \right) \tag{3.7}$$

C_{ijkl}, u_{ij}, ε_{ij}^0 are mechanical stiffness tensor, misfit strain due to substrate film lattice mismatch and self strain due to paraelectric to ferroelectric phase transition, respectively. The self strain due to phase transition can be determined from spontaneous polarization as

$$\varepsilon_{ij}^0 = \begin{pmatrix} Q_{11}P_1^2 + Q_{12}(P_2^2 + P_3^2) & Q_{44}P_1P_2 & Q_{44}P_1P_3 \\ Q_{44}P_1P_2 & Q_{11}P_2^2 + Q_{12}(P_1^2 + P_2^2) & Q_{44}P_2P_3 \\ Q_{44}P_1P_3 & Q_{44}P_2P_3 & Q_{11}P_3^2 + Q_{12}(P_1^2 + P_2^2) \end{pmatrix}. \tag{3.8}$$

Q_{ij} are electrostrictive coefficient tensors, relating second order strain to the first order polarization vectors. When necessary multiplications are implemented one gets the elastic and electromechanical coupling energy in the below form

$$\begin{aligned} F_E = &-\tfrac{1}{2}S_{11}[\sigma_1^2 + \sigma_2^2 + \sigma_3^2] - S_{12}[\sigma_1\sigma_2 + \sigma_1\sigma_3 + \sigma_2\sigma_3] - \tfrac{1}{2}S_{44}[\sigma_4^2 + \sigma_5^2 + \sigma_6^2] \\ &-Q_{11}[\sigma_1 P_1^2 + \sigma_2 P_2^2 + \sigma_3 P_3^2] - Q_{12}[\sigma_1(P_2^2 + P_3^2) + \sigma_2(P_1^2 + P_3^2) + \sigma_3(P_1^2 + P_2^2)]. \\ &-Q_{44}[\sigma_4 P_2 P_3 + \sigma_5 P_1 P_3 + \sigma_6 P_1 P_2] \end{aligned} \tag{3.9}$$

With the modification of dielectric stiffness coefficients by electrostrictive and stiffness coefficients, the combination of F_P and F_E can be written as

$$\begin{aligned} F_{P+E} = &\,\alpha_1^m\left(P_1^2 + P_2^2\right) + \alpha_3^m P_3^2 + \alpha_{11}^m\left(P_1^4 + P_2^4\right) + \alpha_{33}^m P_3^4 + \alpha_{13}^m\left(P_1^2 P_3^2 + P_2^2 P_3^2\right) + \alpha_{12}^m P_1^2 P_2^2 \\ &+\alpha_{111}\left(P_1^6 + P_2^6 + P_3^6\right) + \alpha_{112}\left[P_1^4\left(P_2^2 + P_3^2\right) + P_3^4\left(P_1^2 + P_2^2\right) + P_2^4\left(P_1^2 + P_3^2\right)\right] \\ &+\alpha_{123}P_1^2 P_2^2 P_3^2 + \frac{u_m^2}{S_{11} + S_{12}} \end{aligned} \tag{3.10}$$

where α_i^m and α_{ij}^m are modified dielectric stiffness coefficients with respect to misfit strain and 2D clamping of the thin film and S_{ij} are the elastic compliance factors [34]. Extended forms of these modified dielectric stiffness coefficients can be found in Appendix 1.

In an homogeneous system an external field E conjugated to the order parameter contributes to the free energy by $-EP$ [30]. In ferroelectrics this contribution is defined as electrostatic energy [35]:

$$F_{ELECTRO} = -\left(E_1 P_1 + E_2 P_2 + E_3 P_3\right)$$ (3.11)

Electrostatic energy introduces a linear term to the energy expression that disturbs the degeneracy of otherwise degenerate state for a given uniaxial spontaneously polarized state.

3.3. Ferroelectric Thin Films with Charged Impurities

In this section, the governing equations and boundary conditions for effect of depletion charge impurities on field and temperature dependent characteristics of ferroelectric thin film capacitors are described within the continuum approximation.

3.3.1 Geometry of the Capacitor

The geometry of capacitor system is illustrated in Figure 3.1. The material system considered in this study is epitaxial (001) BaTiO$_3$ (BT) on a (001) SrTiO$_3$ (ST) substrate with pseudomorphic top and bottom metallic electrodes, totally fitting the lattice dimensions of the substrate. A two dimensional grid of 200n x kn cells is created, where n is the unit cell dimension, 200 is the width and k is the height of the thin film cross-section. Width corresponds to x-axis while height corresponds to film thickness and z-axis. It should be noted that even the constructed grid is two dimensional, it satisfies to represent the behaviour of a three dimensional thin film with stripe domain structure along the y-axis (Figure 3.2). So, it is assumed that y-axis behaves just like as x-axis, hence $P_2 = P_1$. This assumption is reasonable in energetic concerns because in this way P_2 is not omitted while the domains stabilize in stripe geometry along y-axis. Within the stripe domain concept, it suffices to consider a two-dimensional system. A checker board domain structure is not energetically favourable due to the high domain wall density in the film.
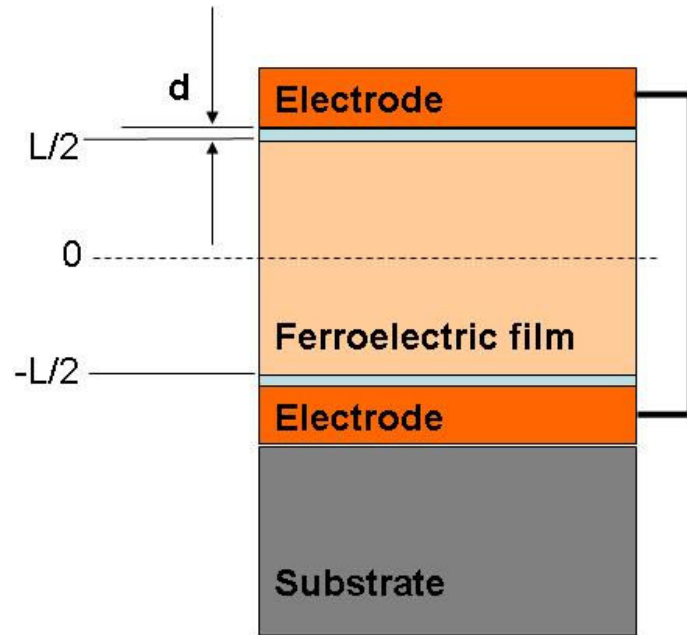
Figure 3.1 Schematic of the simulated ferroelectric thin film capacitor system
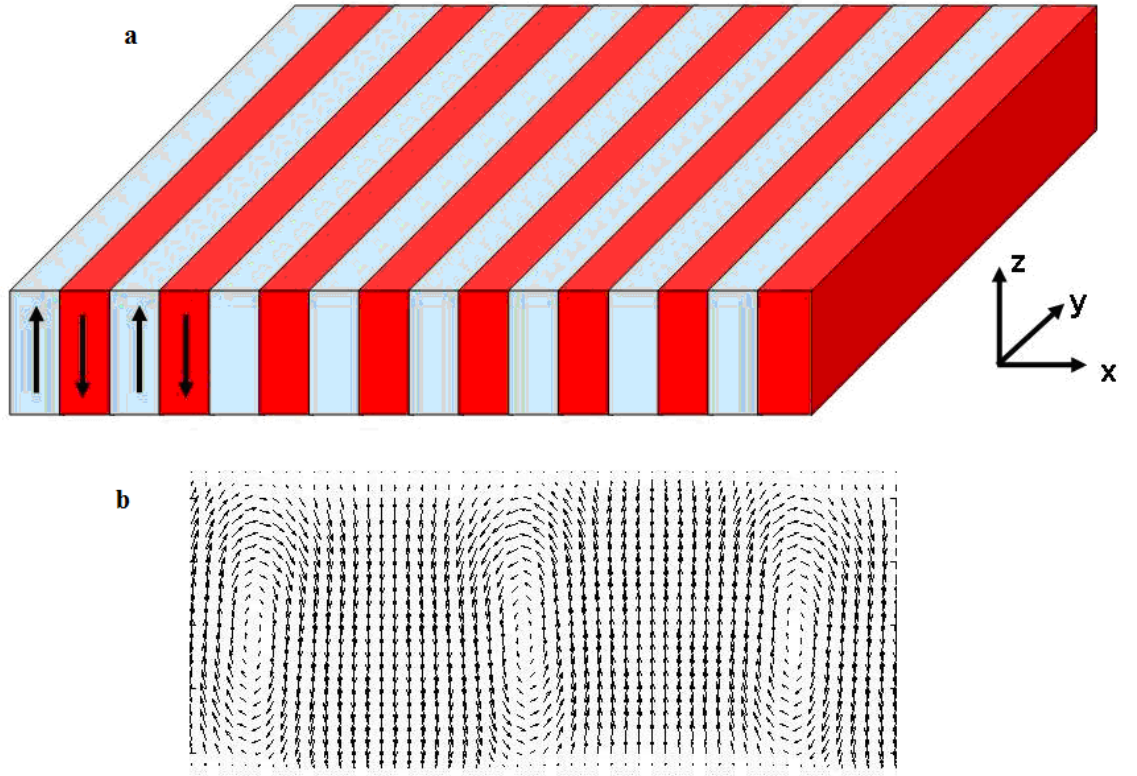
Figure 3.2 a) Stripe domain structure, domains formed on *x-z* plane extends along *y*-axis and b) An *x-z* vector field section of polarization in the domains computed for (001) BaTiO$_3$ strained on (001) SrTiO$_3$.

3.3.2. Equations of State

The system to be studied is partitioned as a ferroelectric layer and a dielectric dead layer by defining a stepwise function, w, to define the interface between the two.

$$w = 1 \; when \; -L/2 \leq z \leq L/2$$
$$w = 0 \; when \; -L/2 - d < z < -L/2 \; and \; L/2 < z < L/2 + d \tag{3.12}$$

Using the above definition of w, total volumetric energy of the ferroelectric thin film with depletion charge densities can be written as

$$F_T = \int_V \left[w(F_0 + F_P + F_G + F_E + F_{ELECTRO}) + (1 - w)F_{DL} \right] dV , \tag{3.13}$$

where dV is the infinitesimal bounded volume of system. F_0, F_P, F_E and $F_{ELECTRO}$ are discussed in the previous section. In this section, gradient energy F_G has to be added into the system energy since the system is not homogeneous due to the depolarizing fields as well as thickness and depletion charge effects. The presence of this term renders abrupt variations of the order parameter unfavourable and allows a smoother variation of the order parameter. The form of this term was proposed in early 1920s by Zernike and was further incorporated into the free energy of various systems, including ferroelectrics to account for fluctuations of the order parameter by V. L. Ginzburg, the details of which will not be discussed here as it is outside the scope of this thesis. Gradient energy for the system of interest includes derivatives of polarization in x- and z-directions only, since in the stripe domain structure, polarizations do not change along y-direction and is written as

$$F_G = -\left(G_{33}\left(\frac{dP_3}{dz}\right)^2 + G_{31}\left(\frac{dP_3}{dx}\right)^2 + G_{13}\left(\frac{dP_1}{dz}\right)^2 + G_{11}\left(\frac{dP_1}{dx}\right)^2 \right) \qquad (3.14)$$

For convenience, gradient energy coefficient is assumed to be isotropic and is taken as $G_{33} = G_{31} = G_{13} = G_{11} = 3\times10^{-10}$. The polarization related energy of the ferroelectric layer (F_{FL}, F_T when w=1) is found by summation of the Eq. (3.10), (3.11) and (3.14) for $P_1 = P_2$:

$$F_{FL} = 2\alpha_1^m P_1^2 + \alpha_3^m P_3^2 + (2\alpha_{11}^m + \alpha_{12})P_1^4 + \alpha_{33}^m P_3^4 + 2\alpha_{13}^m P_1^2 P_3^2 + \alpha_{111}(2P_1^6 + P_3^6)$$
$$+2\alpha_{112}(P_1^6 + P_1^4 P_3^2 + P_3^4 P_1^2) + \alpha_{123}P_1^4 P_3^2 + \frac{u_m^2}{S_{11} + S_{12}} - G_{11}\left(\frac{dP_1}{dx}\right)^2 - G_{13}\left(\frac{dP_1}{dz}\right)^2 \quad (3.15)$$
$$-G_{33}\left(\frac{dP_3}{dz}\right)^2 - G_{31}\left(\frac{dP_3}{dx}\right)^2 - \left(E_1 P_1 + E_3 P_3\right)$$

The energy density of dead layer (F_{DL}, F_T when w=0) is simply

$$F_{DL} = \frac{1}{2}\varepsilon_0\left(E_1^{\,2} + E_3^{\,2}\right) \qquad (3.16)$$

Minimization of Eq. (3.13) for w=1, yields the following Euler-Lagrange relations

$$\frac{\partial F_T}{\partial P_3} - \frac{\partial}{\partial z}\left(\frac{\partial F_T}{\partial f_1}\right) - \frac{\partial}{\partial x}\left(\frac{\partial F_T}{\partial f_2}\right) = 0 \qquad (3.17)$$

$$\frac{\partial F_T}{\partial P_1} - \frac{\partial}{\partial z}\left(\frac{\partial F_T}{\partial f_3}\right) - \frac{\partial}{\partial x}\left(\frac{\partial F_T}{\partial f_4}\right) = 0 \qquad (3.18)$$

with $f_1 = dP_3/dz$, $f_2 = dP_3/dx$, $f_3 = dP_1/dz$ and $f_4 = dP_1/dx$.

The equations of state are then derived from Eq.(3.17) and (3.18) as:

$$w(2\alpha_3^m P_3 + 4\alpha_{33}^m P_3^3 + 4\alpha_{13}^m P_3 P_1^2 + 6\alpha_{111}P_3^5$$
$$+\alpha_{112}(4P_3 P_1^4 + 8P_3^3 P_1^2) + 2\alpha_{123}P_3 P_1^4 - G_{33}\frac{d^2 P_3}{dz^2} - G_{13}\frac{d^2 P_3}{dx^2}) + (1-w)\frac{D_3}{\varepsilon_r \varepsilon_0} \qquad (3.19)$$
$$= wE_3 + (1-w)E_3$$

$$w(4\alpha_1^m P_1 + 4(2\alpha_{11}^m + \alpha_{12}^m)P_1^3 + 4\alpha_{13}^m P_1 P_3^2 + 12\alpha_{111}P_1^5 +$$
$$4\alpha_{112}[3P_1^5 + 2P_1^3 P_3^2 + P_1 P_3^4] + 4\alpha_{123}P_1^3 P_3^2 - G_{31}\frac{d^2 P_1}{dz^2} - G_{11}\frac{d^2 P_1}{dx^2}) + (1-w)\frac{D_1}{\varepsilon_r \varepsilon_0} \qquad (3.20)$$
$$= wE_1 + (1-w)E_1$$

Until here, the derivation of the free energy and equations of state for the specific system is described. However, in order to find the equilibrium value of polarization at a given state, the electrostatic equations should also be satisfied and the potential distribution inside the capacitor should be found. For this purpose, now, boundary conditions to solve the Maxwell equations and dependence of potential on ferroelectric polarization will be given.

3.3.3. Electrostatics of the System and Boundary Conditions

In this study, phase transition temperatures of the FE thin films are computed in the absence of external electric field. Dirichlet boundary conditions [36] for no bias situation requires zero potential at the top and bottom electrode-film interface given as:

$$\phi = 0 @ z = \pm(L/2 + d) \qquad (3.21)$$

The $\phi = 0$ condition corresponds to the total charge compensation at the electrode-film interface. The flow of negative charges from semiconductor to metal does not create any potential drops since the metal itself has already got a sea of electrons. Therefore,

immediate compensation of the diffused charges take place. The electric field can then be calculated from the gradient of potential in both x and z directions and for both ferroelectric and dead layer:

$$E_1 = -\frac{\partial \phi}{\partial x}, E_3 = -\frac{\partial \phi}{\partial z} \qquad (3.22)$$

The electrostatic potential in each grid is calculated by solving Maxwell equation in the absence of free charges as $\nabla \cdot \boldsymbol{D} = 0$ and in the presence of depletion charges due to ionized impurities as $\nabla \cdot \boldsymbol{D} = \rho$. Calculation of the dielectric displacement vector is carried out separately in the dead layer and the ferroelectric thin film. Dielectric displacements for the dead and ferroelectric layers are

$$D_i^d = \varepsilon_r^d \varepsilon_0 E_i^d \quad (i = 1,3) \qquad (3.23)$$

$$D_i^F = \varepsilon_b \varepsilon_0 E_i^F + P_i \quad (i = 1,3). \qquad (3.24)$$

respectively. The dead layer is assumed to be isotropic and has a dielectric constant of $\varepsilon_r^d = 20$ for this thesis. ε_b, background dielectric constant, is assumed to be 5 and is inserted into the system to exemplify the dielectric component of polarization apart from the ferroelectric component; namely P_1 and P_3 in the equation of state. One must note that the potential drops in the dielectric and the ferroelectric layers are different. Writing Eq.(3.23) and (3.24) explicitly one gets

$$\frac{\partial^2 \phi}{\partial z^2} + \frac{\partial^2 \phi}{\partial x^2} = -\frac{\rho}{\varepsilon_r^d \varepsilon_0} \qquad (3.25)$$

for dead layer and

$$\frac{\partial^2 \phi}{\partial z^2} + \frac{\partial^2 \phi}{\partial x^2} = \frac{1}{\varepsilon_b \varepsilon_0} \left(\frac{dP_3}{dz} + \frac{dP_1}{dx} - \rho \right). \qquad (3.26)$$

for the ferroelectric layer. Finite difference discretization is applied to solve the electrostatic potentials while keeping the unit cell dimension in x-direction, dx, equal to unit cell dimension in z-direction, dz, for convenience. Details of discretization of spatial derivatives are listed in the Appendix 1.

As can be followed from the Figure 3.3, after the potential is calculated using Eqs. (3.25) and (3.26), electric field is calculated using these potential values. Subsequently, ferroelectric polarization is found from the modified Landau-Ginzburg-Devonshire (LGD) equation of state coupled with interface boundary conditions and presence of depletion charges. Ferroelectric polarization is deduced from the discretized equations of state, namely Eq.(3.19) and Eq.(3.20) by keeping that polarization term at one side of the equation while gathering all the rest of the terms on the other side of the equation. Details of the derivation can be checked from the Appendix 1.

Boundary conditions for polarization at the top and bottom ferroelectric-electrode interface are

$$\left[P_i + \lambda \frac{dP_i}{dz} \right]_{z=-\frac{L}{2}-d,\frac{L}{2}+d} = 0 \ (i = 1,3), \tag{3.27}$$

where λ, extrapolation length is taken as infinite, i.e., there is no reduction or gain in polarization values at the film-metal interface. On the other hand, along the x-axis, periodic boundary conditions are applied in order to simulate an infinite width of slab as

$$P_i(x=1) = P_i(x=199), \ P_i(x=2) = P_i(x=200) \quad (i=1,3) \tag{3.28}$$

Using a Gauss-Siedel iterative scheme, final value of polarization is obtained as the difference between consecutive iterations goes to as low as 10^{-8} for polarization in the ferroelectric layer. This corresponds to about 5000 iterative steps. The new polarization value obtained by Eq. (A1.1)/(A1.2) is inserted into Eq. (3.26) in each iteration, therefore both polarization and potential are updated in each iteration.

Owing to the compressive in-plane misfit in (001) BaTiO$_3$ on (001) SrTiO$_3$ (about 2.5 %), only P_3 is the spontaneous polarization. In addition, when depletion charge exists, P_3 also contains the built-in polarization, P_b. Thus, from here onwards the ferroelectric part of P_3 will be denoted as P_f and the built-in part will be expressed as P_b. Note that when $\rho=0$, there is only one solution which is $P_3 = P_f$. On the other hand, P_1 indicates linear polarizability along the in-plane of the film, i. e., P_1 has zero solution in the absence of any electric field.

31

3.3.4. Details of Simulation Procedure

Cell dimension of the grid is taken as 4 Å similar to well known pseudocubic perovskites such as BT to imitate the order of lengths at which polarization can vary in the system compared to real systems. That is why grid size has not been varied but has been fixed to a constant value. Dead layer, when present, is inserted into the system manually as being 1 unit cell thick (d=1) for this thesis. Another statement is that each impurity, contributing to charge density ρ, has only one positive unit charge (1.602x10^{-19} C) in all cases and the depletion charge density is assumed to be constant throughout the film, i.e., the impurity charges homogeneously distribute themselves inside the film. This also means that the entire film is thin enough to be counted as depletion layer. On the other hand, the entire "capacitor system" is neutral as the negative charges previously splitted from ionized impurities, whose density is ρ, accumulate on the electrodes, meaning there is no external charge injection or extraction from the capacitor system.

For the polarization maps, we gradually reduced to the room temperature by initiating from high temperature such as 600 °C that is around the Curie temperature. At each temperature step, we simultaneously solved the equations of state and electrostatics with 5000 iterations. The schematic flow of the iteration can be seen from Figure 3.3 as well.

In order to extract polarization wavevector plots, the data are taken separately for each thickness at room temperature. Proverbially, the domain shapes transform from sinusoidal waves at high temperature to square patterns as the temperature is reduced. However, the domain periods do not change in the middle of the z-axis. The length of a domain period is measured as a sum of the lengths along x-axis of two opposite signed domains for the case of numerical results. On the other hand, analytical results have been extracted by finding the value of polarization wavevector for the minimum value of A in Eq. A2.6 where phase transition takes place.

Phase transition temperatures are found by implementing a cooling run procedure for each film thickness and charge density while tracing the total of absolute value of the polarization. Total absolute value of polarization abrubtly falls to zero at the phase

transition point from ferroelectric to paraelectric state. In order to obtain a clear trend, film thickness interval is chosen as small as 4 nm and a thickness range of 4 nm to 24 nm is investigated.

Hysteresis simulations are performed at room temperature but an external field cycle is created by changing the potentials at the top and bottom electrodes. Therefore, the variable in the flowchart of Figure 3.3 is not the temperature but the potential at the electrodes in this case. Naturally, the boundary condition that is obliging zero potential at the electrodes is not valid for these simulations. Initially, with a 0.1 V increment, top electrode potential is raised to 1 V and bottom electrode potential is decreased to -1 V, simultaneously. Then, the process is reversed; , top electrode potential is decreased to -1 V and bottom electrode potential is raised to 1 V, simultaneously. Finally all the potentials are brought to zero again.
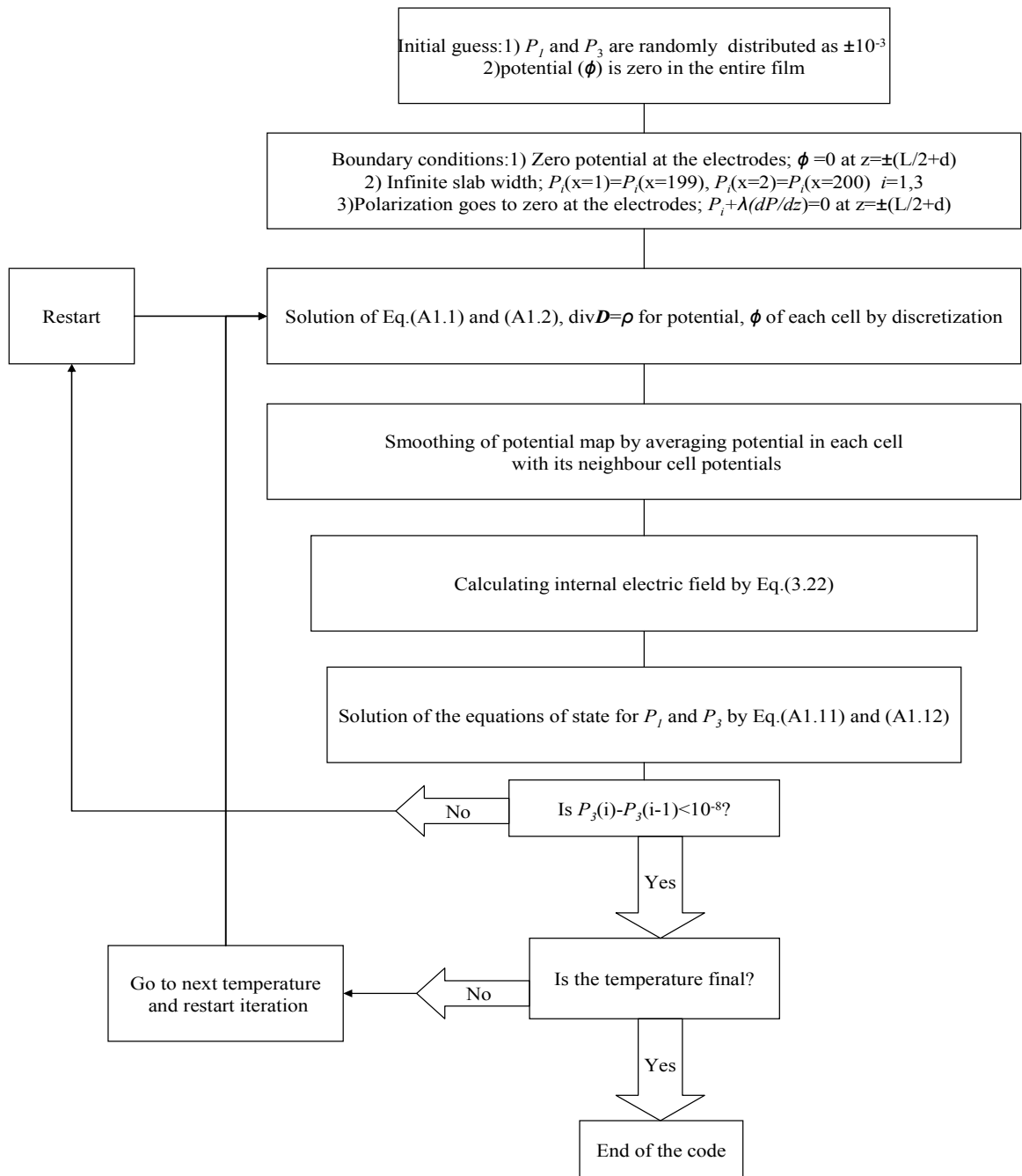
Figure 3.3. Flowchart of the coupled solution of potential and polarization in the ferroelectric thin film capacitor

CHAPTER 4

RESULTS AND DISCUSSION

4.1 Room Temperature Domain Structures for Thin Films with Ideal Electrodes

In the presence of ideal electrodes (where field cannot penetrate the electrode), the dielectric dead layer is absent and d in Figure 3.1 is considered to be zero. The results obtained at room temperature (RT) are extracted from three different film thicknesses, 12 nm, 16 nm and 20 nm in order to observe a trend as a function of film thickness for the fully depleted film thickness range. Ionized impurity densities considered in this work are 5×10^{25} impurities/m^3 for moderate-high and 2×10^{26} impurities/m^3 for high density limit. The films thinner than 10 nm with depletion charge at maximum density limit are always found to exist in an imprinted single domain state (See Figure 4.1) which is a consequence of relatively less strong built-in field that is unable to break the homogeneous nature of the film. If it was inhomogeneous, the built-in field effect would be so strong that the local phase transition temperature would depend on the built-in electric field at each particular location. In the absence of depletion charges the same thin films also exist in an homogeneous monodomain state that is consistent with the conclusion of ineffectiveness of built-in field in creating inhomogeneity throughout the thickness of the film. However, the main focus of this thesis has been the conditions that do trigger domain structures.
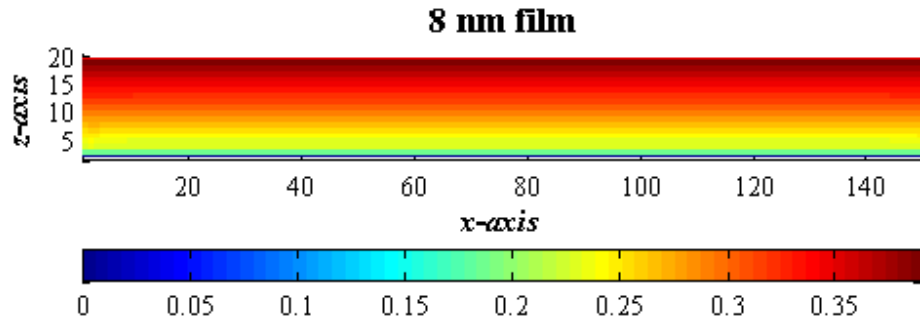
Figure 4.1. RT single domain polarization for 8 nm film without dead layers and with high depletion charge density

(a)

(d)

(b)

(e)

(c)

(f)
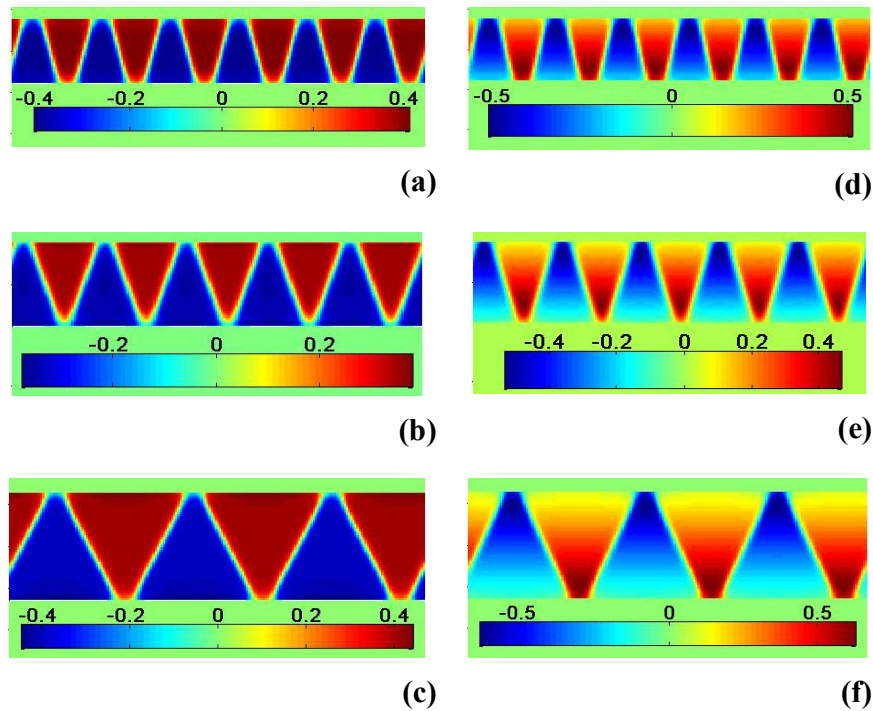
Figure 4.2. The RT domain total polarization configurations of the (a) 12 nm, (b)16 nm and (c) 20 nm thick films with 2×10^{26} ionized impurities/m^3 and the extracted ferroelectric polarization given for (d) 12, (e)16 and (f) 20 nm thick films on the right hand side. Scales are given to display the range of P_3 in C/m^2.

36

Figure 4.2 demonstrates domain structures that form within films of several thicknesses that have the same volumetric depletion charge density corresponding to 2×10^{26} impurities/m^3. Low charge densities of these thicknesses have also yielded only a unidirectional P_f. The amplitude of this uniaxial P_f is less in one half of the film than in the other half concomitant with the internal field distribution. In Figure 4.2, a,b and c images show the total polarization which include both ferroelectric and built-in polarization parts while d,e and f show only FE component of polarization which is obtained by subtracting P_b from P_3 for 12, 16 and 20 nm films. P_b is obtained by running the simulation above the Curie point where the whole system is in the paraelectric state. Obtaining P_b at a higher temperature does not create inconsistency because it is nearly temperature insensitive and it is the only solution satisfying Eq. (3.19)-(3.20) and Eq. (3.25)-(3.26) at high temperature. A saw-tooth type domain structure with a thickness dependant period is clear in this depletion charge density and thickness interval at RT. As can be seen from Figure 4.3, the internal built-in field goes to higher values at the electrodes as the film thickness increases. Therefore the formation of domains in thicker films is due to the highly inhomogeneous nature of the built-in field renormalizing the linear term in P_3 in Eq. (3.19). Thus, for a constant depletion charge density, the built-in field creates more profound variations in local transition temperatures towards film boundaries with increasing thickness. Hence thicker structures are forced to undergo domain stabilization to minimize the depolarizing field emanating from the inhomogeneous depletion charge field. The domain period is not a constant value but a function of position along z- axis since the inhomogeneous depletion charge field imposes a depolarizing field at a different strength at each point along z-axis.
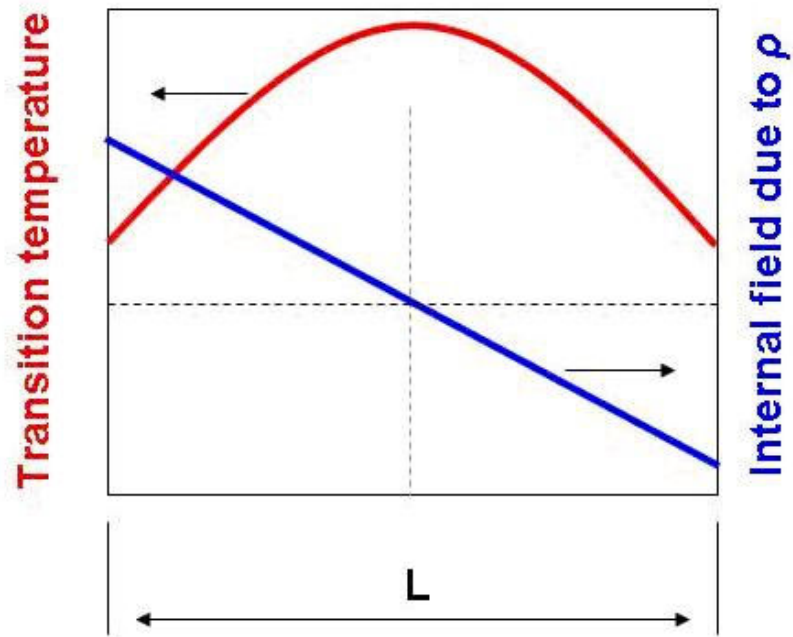
Figure 4.3. Schematic of the built-in field plotted as a function of position along the thickness of the ferroelectric film for a given homogeneous charge density (Right axis). The red curve indicates the variation of the Curie point along the thickness due to the built-in field.

4.2 Room Temperature Domain Structures for Thin Films with Dead Layer

In the presence of both dead layer (d=1) and depletion charge, a competition between the two forces determine the final domain structure.
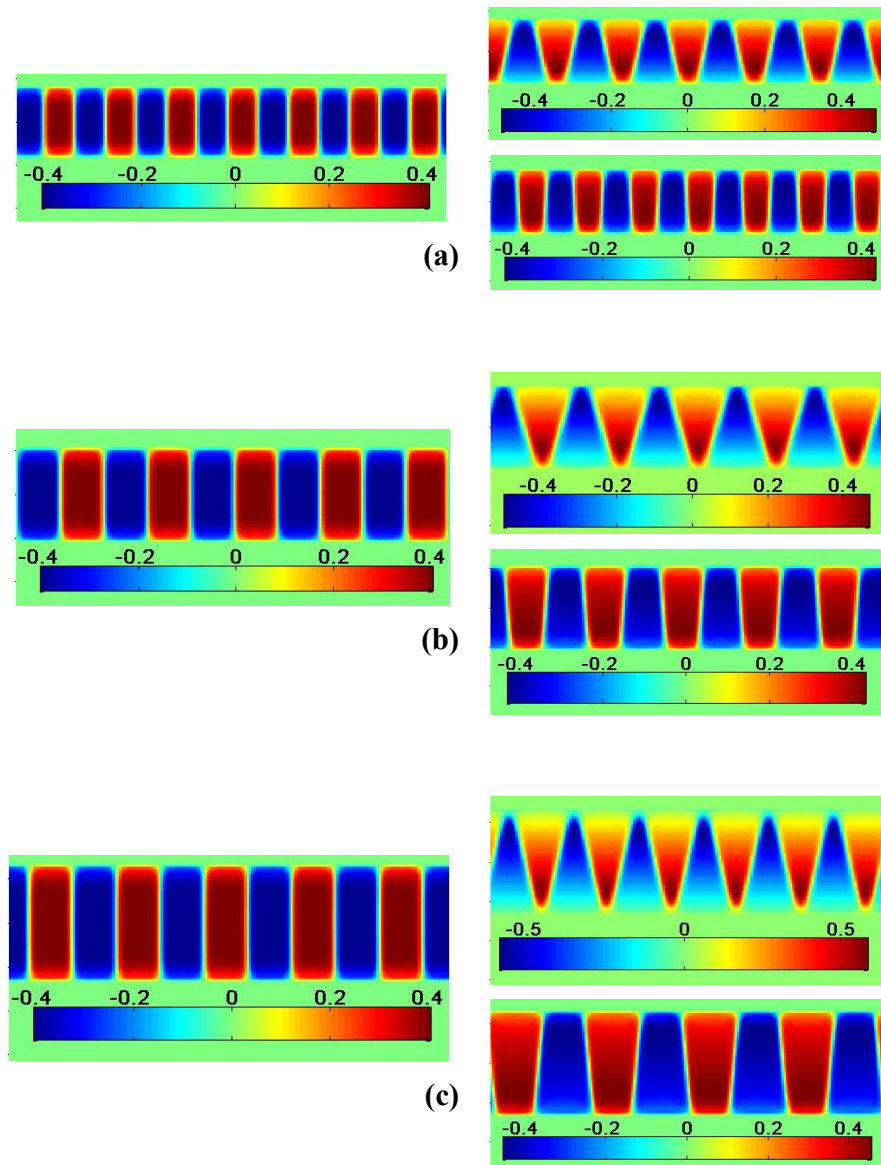
Figure 4.4. Domain structures for (a) 12 nm, (b) 16 nm and (c) 20 nm thick films with dead layers. The right hand side of each colormap for a given thickness are the domain structures for $\rho=2\times10^{26}$ (Upper colormap) and $\rho=5\times10^{25}$ (Lower colormap). Scales are given to display the range of P_3 in C/m^2.

In Figure 4.4, left hand side displays the domain structures formed in the absence of depletion charges and presence of dead layer, right hand side displays the domain structures formed in the presence of both depletion charges and dead layer. Upper colormap on the

right hand side is for depletion charge density $\rho= 2\times10^{26}$ and lower one is for $\rho= 5\times10^{25}$. It can be observed that moderate charge density of $\rho= 5\times10^{25}$ slightly alters domain wall angles with respect to depletion charge free films while higher charge densities constrain the saw-tooth like domain structure with a prominent maxima of P_f at the domain tips again. Taking into consideration of longer domain wall length in angled domain walls, the suppression of depletion charge field can be said to overcome the effect of domain wall energy. Also, it is interesting that as the film thickness increases, the domain tips get sharper, indicating that with high depletion charge densities, films are under weaker influence of dead layers.

Before discussing the probable changes in domain period when depletion charges are present in thin films, the results for the domain wave vector, k, obtained both from MATLAB simulations and using the approach presented in [37] are given to validate the trends of the simulations for charge-free films in Figure 4.5a. A summary of the approach of [37] in a modified form (See also [38]) is given in the Appendix 2 for convenience. Arising from the numerical nature of the simulation study and the finiteness of the system investigated (despite periodic boundary conditions along the film plane), a smooth and gradual change in the domain period, hence in k is not attained. Still, there is an excellent agreement with the results obtained using the methodology in the Appendix 2. Note the approach in the Appendix 2 adopted from [37] and [38] analyzes the phase transition point considering linear equation of state. The domain period is found to be not changing at all with further cooling upon the transition from the paraelectric to the multidomain FE state and transforming from a sinusoidal pattern to a square-like one, making it feasible to compare k values at and below the transition. In other words, even when the simulation temperatures are not the same as the temperatures at which the k values were found using the approaches in [37] and [38], the k's in both their study and the simulations are directly comparable.
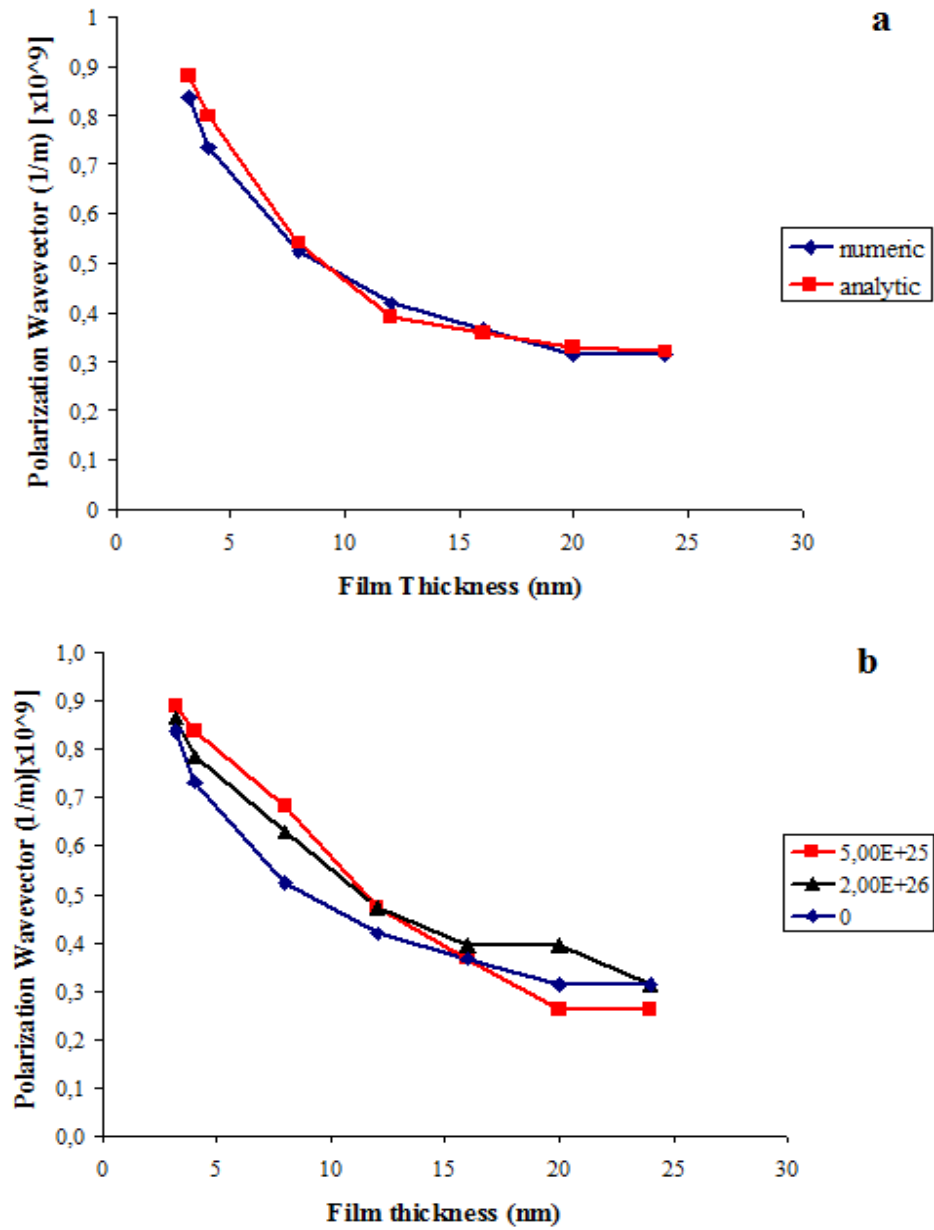
Figure 4.5. a) Wave vector of the polarization along the film plane as a function of film thickness at the transition derived from solving Eq. (A2.16) for the point of loss of stability of the paraelectric phase summarized in the Appendix 2 (red curve) and the wave vector we found in our simulations (blue diamonds) for d=1 unit cell. b) Wave vector of the polarization along the film plane as a function of thickness for films without charge (blue curve with diamonds), films having 5×10^{25} ionized impurities/m^3 charge density (red curve with squares) and films having 2×10^{26} ionized impurities/m^3 charge density (black curve with triangles) for d=1 unit cell.

To visualize the impact of depletion charge on the domain structures in films with dead layers, the behavior of the wave vector, k of the P_f wave plotted as a function of film thickness for ionized impurity densities of $5x10^{25}$ and $2x10^{26}$ /m^3 is discussed. The results for films at RT without and with depletion charge are in Figure 4.5b. The presence of electrical domains in films with depletion charge have persisted for the entire thickness range of interest in this study. When present, the depletion charge density was kept constant at $5x10^{25}$ and $2x10$ ionized impurities/m^3 for the sake of demonstration. Domain period for films thinner than 12 nm with $5x10^{25}$ ionized impurities/m^3 is smaller than the charge-free film, while films with $2x10^{26}$ ionized impurities/m^3 follow similar trend with the charge-free film but with slightly larger k values. The general trend of the increase in k values for films thinner than 12 nm in this work might be perceived as an indication that the depletion charge amplifies the depolarizing field for a given set of material parameters (domain wall energy, fixed dead layer thickness and dielectric constant and etc.). But this trend changes with increasing film thickness for the films having $5x10^{25}$ ionized impurities/m^3 with respect to the charge-free case. Around 15 nm, a crossover occurs after which the thicker films with $5x10^{25}$ ionized impurities/m^3 carrier density develop a coarser domain structure. Here, from the data of MATLAB simulations, it can be seen that as the film thickness is reduced, the domain period is altered in a way that the depolarizing field appears to be amplified, leading to a finer domain period hence a larger k. Still, it is not possible to arrive at general conclusions for the entire thickness regime considered because thicker films (>16 nm) with moderate depletion charge density has a distinctly different domain period.

Despite the thought that any formation giving rise to or amplifying depolarizing fields will reduce the transition temperature, comparing the k values for a given thickness does not lead to conclude so. To analyze the effect of depletion charge effects on the transition temperature, we carry out cooling runs in the simulations, extract and discuss the transition temperatures in the next section.

4.3 Phase Transition Temperatures

The bulk transition temperature for (001) BaTiO$_3$ fully strained on (001) SrTiO$_3$ is

652°C which is the calculated value when all couplings of 2D clamping to polarization is included to phase transition considerations as shown in Eq. A2.6 of Appendix 2. The paraelectric-ferroelectric transition temperature for FE thin films is expected to be lowered in the presence of depletion charges, dead layers or when both coexist. Film thickness importantly comes into play in all of the cases above. Here the emphasis is on the situation when dead layers and depletion charges are both present but also a case where the films at a thickness range of 3.2 nm to 24 nm have ideal electrodes is studied for comparison. For reference, the transition temperature is first computed as a function of film thickness for a fixed dead layer thickness (d=1) and dielectric constant (ε_r=20) and the results are displayed in Figure 4.6 along with the results obtained using the method prescribed in the Appendix 2. The transition temperatures are found by tracking $<|P_3|>$ in the simulations. The transition temperatures computed from the numerical solution of Eq. A2.16a in Appendix 2 has a very good match with the simulation results presented in this work, again confirming the validity of the prescribed method in Chapter 3. It must be borne in mind that the approach of [37] excludes gradient of P_3 (total polarization) along the thickness of the film, i.e. z-axis, which is actually included in this study. This can be the possible cause of the slight deviation between the two results at small thicknesses. As expected, decreasing film thickness results in a reduction of the transition temperature with domain period subsequently becoming comparable or larger than the film thickness.
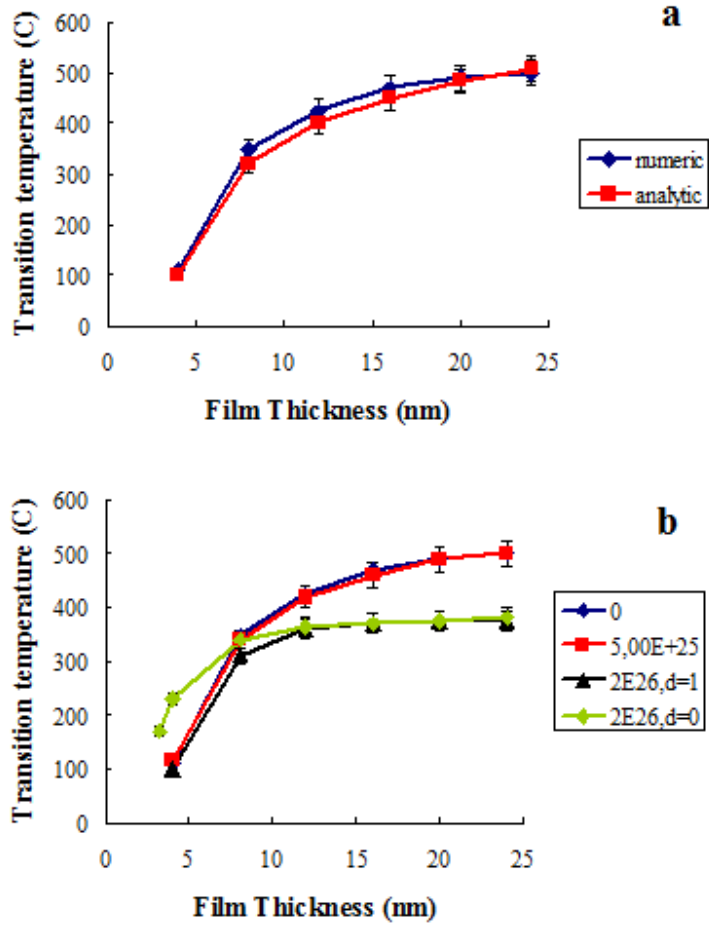
Figure 4.6. Phase transition temperatures in films with dead layers as a function of thickness (a) Results of MATLAB simulations (blue) and solution of Eq. (A2.16) (red) for charge-free films (b) Results for charge-free (blue curve with diamonds), 5×10^{25} (red curve with squares), 2×10^{26} ionized impurities/m^3 depletion charge (black curve with triangles) and the case of d=0 with 2×10^{26} ionized impurities/m^3 (the green curve with diamonds).

Computing the phase transition temperatures in films with dead layers but now with two different depletion charge densities, it is seen from the strong overlap of the curves that films with a charge density of 5×10^{25} ionized impurities/m^3 have nearly the same transition temperature compared to the charge free ones for a given thickness (See Figure 4.6b). Note that a homogeneous charge distribution does not lead to any net bias fields between the electrodes and no smearing of the transition exists, meaning the transition temperature is sharp. Then, the cooling runs for films having a depletion charge density of 2×10^{26} ionized

impurities/m^3 both in the presence and absence of dead layers are carried out to detect the transition. As mentioned previously, tracking $<|P_3|>$ and comparing it with $<P_3>$ allows detecting the phase transition if it is into a multidomain state. These films with 2×10^{26} ionized impurities/m^3 and dead layers have a similar trend with the charge-free films at small thickness but then the transition temperature is significantly reduced for thicker films. Moreover, the transition temperatures in thicker films with and without dead layers are nearly the same. This scenario is certainly different for thinner films (<12 nm) and it is seen that the dead layers entirely dominate the transition characteristics (Compare the curves for the films having 2×10^{26} ionized impurities/m^3 with and without dead layers in Figure 4.6b). This is solely due to the "degree of induced inhomogeneity" in the thicker films where the built-in electric field due to depletion charges induces a strong gradient of the transition temperature via normalization of α_3^m in Eq.(3.15), causing a larger amplitude variation of P_f, possibly overriding dead layer effects. Therefore, a quantitative evidence that the thicker films will be under a stronger influence of the depletion charge effects compared to thinner ones becomes provided. One must remember here, however, that the case of rather high densities of depletion charge is discussed. For moderate-to-low densities (<10^{25} ionized impurities/m^3 in this work), the above discussion on transition temperatures merely converges to discussion of dead layer effects on the transition temperature as a function of film thickness.

4.4. Hysteresis Loops

In a ferroelectric capacitor system there is no internal field when the electrodes are ideal conductors and when the film is pure, i.e., clear of ionized impurities, then, the ferroelectric performs perfectly under external field cycle. However, in real life, depletion charges and dead layers are inevitable. Their effect on coercive field and remnant polarization are discussed in this section. Hysteresis loops for several combinations of dead layer, thickness and depletion charge densities are shown on Figure 4.7 through Figure 4.10. The first comparison is for the effect of depletion charge densities on films with ideal electrodes, i.e., without dead layers (d=0). It can be tracked from Figure 4.7 that moderate

charge density does not destroy hysteresis loop of the 16 nm film but decreases the coercive field compared to the charge-free film which is a sign of depolarizing field of these charges. The charges are acting as nucleation sites for domains of reverse polarization, therefore the energy required to switch such a film gets smaller compared to the energy required to switch a unidirectional collective polarization. In the case of high depletion charge density we observe the remanency loss along with a lower saturation polarization. This indicates a domain wall motion commensurate with the external bias which also means that reverse domains never completely disappear even at high external fields since the internal built-in field is strong enough to keep them stable.

Figure 4.8 represents hysteresis loops of the films with dead layers. In this case there is not much of a difference between charge-free and moderately charged films as seen from the overlap of the loops. Compared to the previous figure, a significant coercive field decrease is already present in the charge-free film which supports that depolarizing field due to incomplete screening of charges has led to an ease of polarization switch. The almost identical loops of blue and red lines are also an evidence of rather homogeneous and weak nature of built in field in moderate charge density. On the other hand the green line of the film with high density ionized impurities does not show a significant difference from the ideal electrode case except a slight change of initial polarization. Also one would expect double loop hysteresis due to the multidomain structure at zero bias during the switching of the electric field from positive to negative for the case of depletion charge free dead layered thin films. The reason for not observing such a double loop behaviour is actually a artifact of the numerical method which does not easily prefer thermodynamically stable phase but gets trapped in a metastable state on the run. We give the hystereses to allow an understanding of the *P-E* behaviour for the single domain state behavior. Single domain states have been previously reported for systems with depletion charge and we find this comparison useful. Very large depletion charge densities, however, push the system into ultimate multidomain stability, which is definitely stable, resulting in a linear response.

Hysteresis simulations of thinner films show similar trends as shown on Figure 4.9 and 4.10. The influence of less inhomogeneous built in field for thinner film expresses itself as overlapped hysteresis loops of charge-free and moderately charged films without

dead layers in Figure 4.9. Decreased coercive field is a sign of extra depolarizing field of dead layer in Figure 4.10 similar to Figure 4.8. On the other hand, for the case of depletion charge free and ideal electroded cases, film thickness does not significantly affect the coercive field as can be observed from these results. For this case, the coercive field of 16 nm film with ideal electrodes becomes $-10,26 \times 10^7$ V/m; very close to the coercive field of 12 nm film with ideal electrodes which is $-8,62 \times 10^7$ V/m. Slight difference can be attributed to the discrete nature of numerical simulation which directly depends on the step size of the electric field cycle.
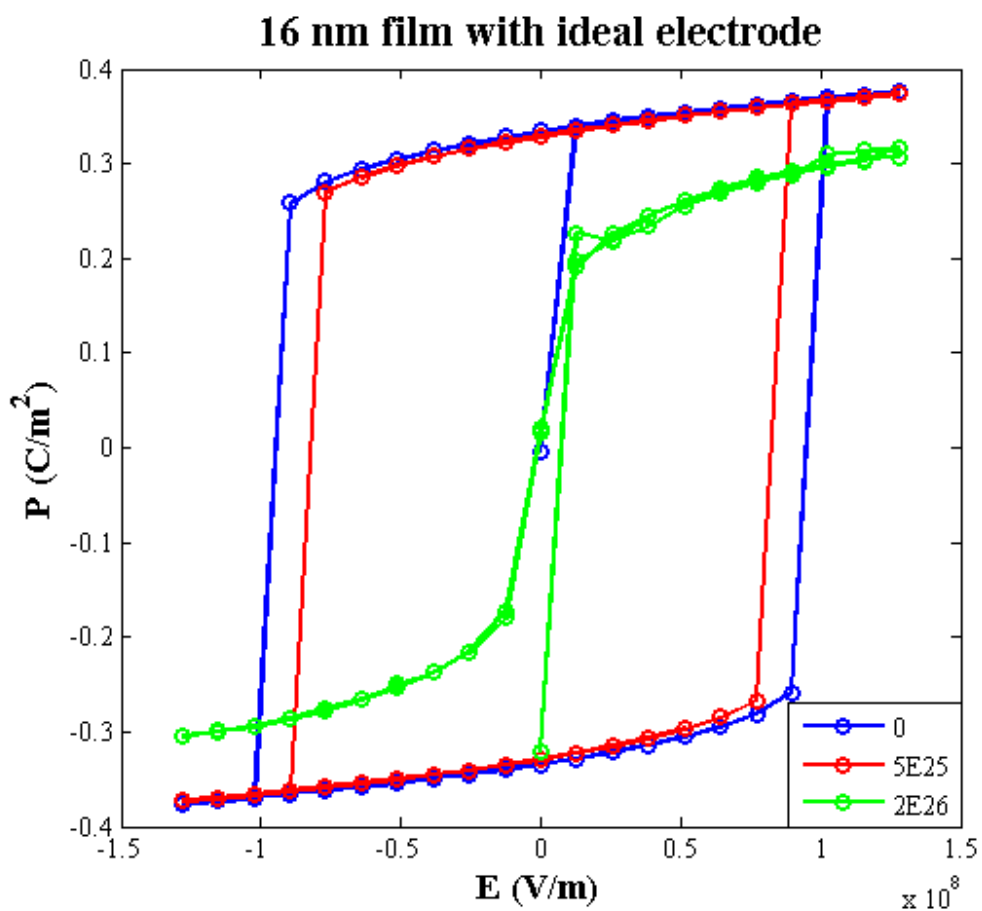
Figure 4.7. Hysteresis simulation of 16 nm film without dead layers for 0 (blue), 5×10^{25} (red) and 2×10^{26} (green) ionized impurities/m^3.
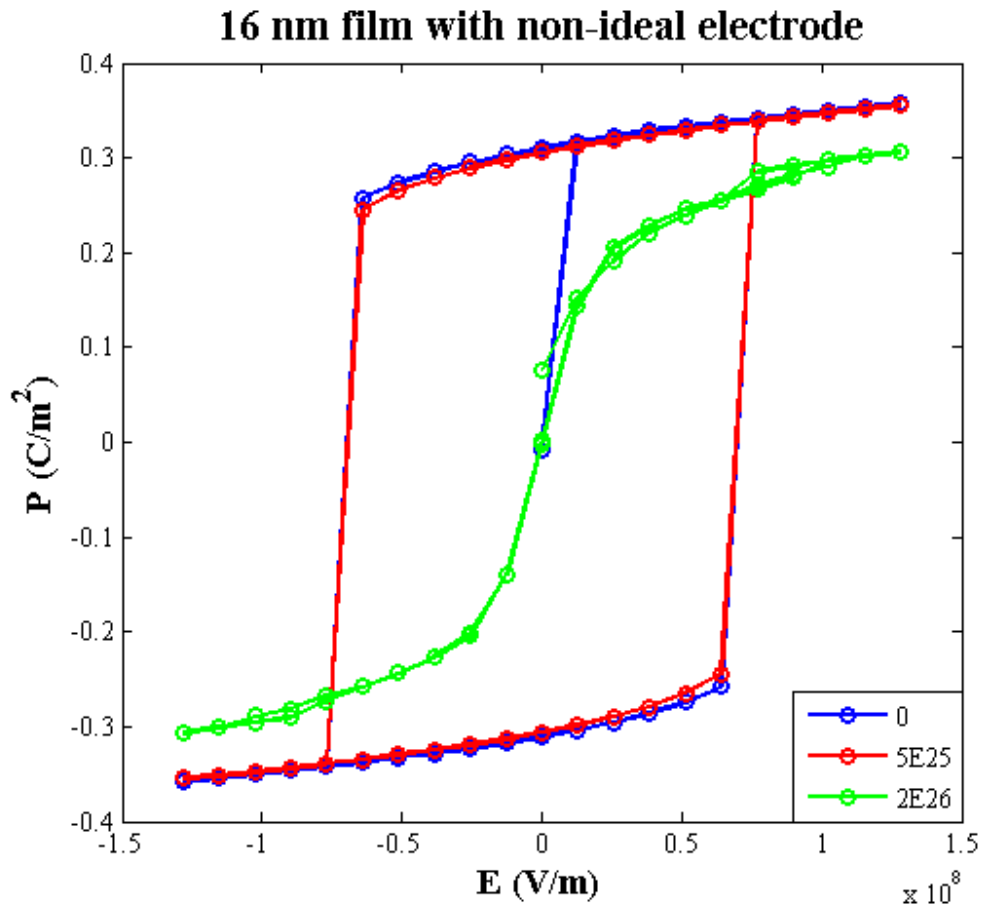
Figure 4.8. Hysteresis simulation of 16 nm film with dead layers for 0 (blue), 5x10²⁵ (red) and 2x10²⁶ (green) ionized impurities/m³.
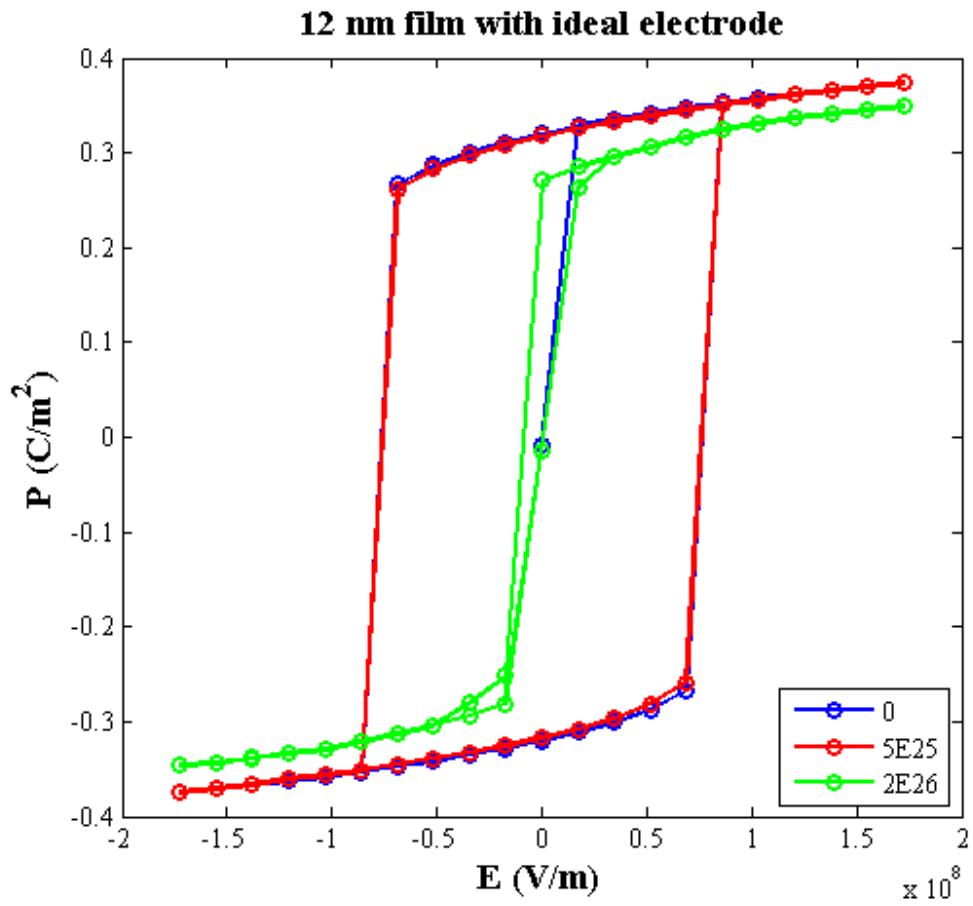
Figure 4.9. Hysteresis simulation of 12 nm film without dead layers for 0 (blue), 5×10^{25} (red) and 2×10^{26} (green) ionized impurities/m^3.
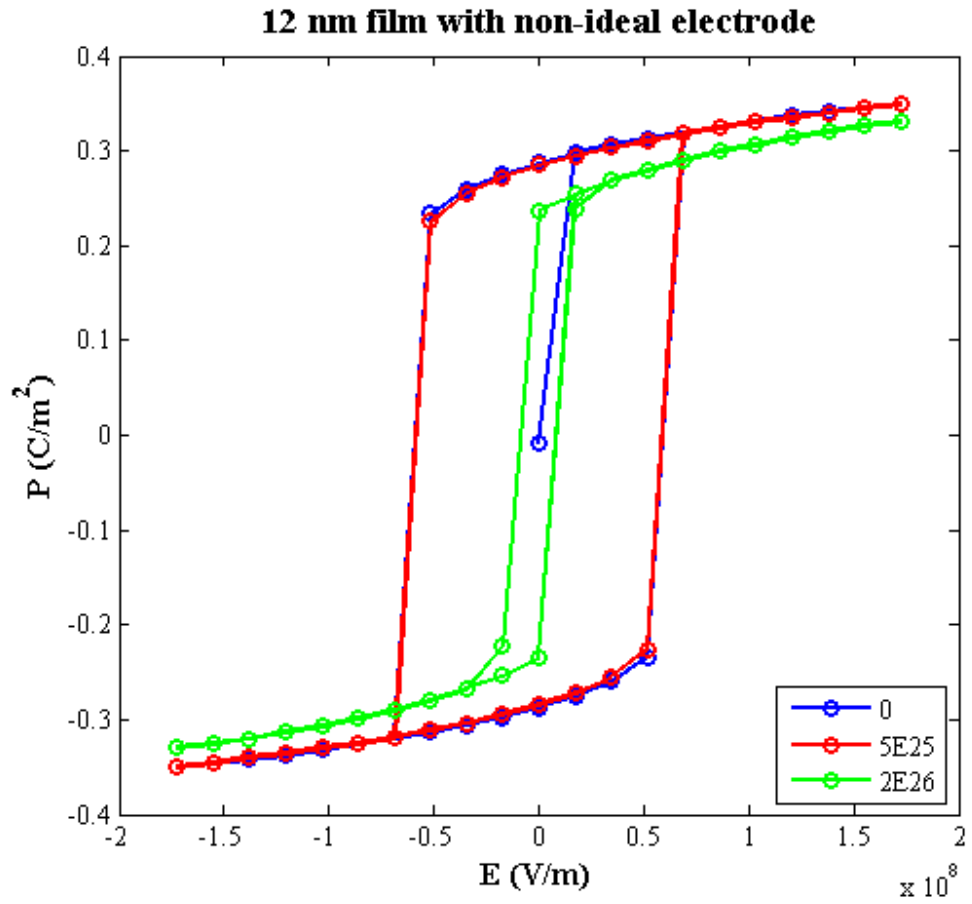
Figure 4.10. Hysteresis simulation of 12 nm film with dead layers for 0 (blue), 5×10^{25} (red) and 2×10^{26} (green) ionized impurities/m^3.

CHAPTER 5

CONCLUSION

5.1 Conclusion

In conclusion, domain formation, phase transition and hysteresis loop characeristics of ferroelectric thin films under homogeneous depletion charge densities and dead layers are investigated in this study. Comparison of the results of numerical to the results of analytical approach showed an appropriate match between results. Eventually, for the first time it is explicitly shown that the existence of inhomogeneous built-in field created by homogeneously distributed depletion charges induce a depolarizing field inside the film which yields a saw-tooth type domain structure even in the absence of dead layers. The inhomogeneous built-in field should also cause a variation in phase transition temperatures throughout the film thickness due to the changing value of the field at each point along the z-axis. On the other hand dead layers at the electrode - film interface also induce depolarizing field to the ferroelectric but dead layer induced depolarizing field creates square domains since its value is constant at each point along the z-axis. So, our results show the domain structures in the cases of depletion charges, dead layers and both of them. In the case of both dead layers and depletion charges, a tilt of square domains is observed for moderate depletion charge densities and saw-tooth domain domination is observed for

high depletion charge densities.

Later on, domain widths are investigated via both numerical simulations and analytical calculations. It has been shown that in the presence of dead layers and for moderate and high density of depletion charges, there is a general decreasing trend for domain width with the reduction in film thickness. However, unfortunately, a clear correlation between depletion charge density and domain width can not be extracted from our results. For a given depletion charge density, the domain width narrows as film thickness reduces due to the amplification of depolarizing field from a relatively more homogeneous built-in field for thinner films.

Phase transition temperature studies have shown that phase transition point is similar for small thickness films with dead layers regardless of the depletion charge density. As the film thickness is increased, higher depletion charge densities contribute to a lower increase in phase transition temperature as opposed to the charge free films where phase transition temperature is significantly higher than thinner films. Moreover, for the high depletion charge density films, the dead layer-free simulation showed a different trend in lower film thicknesses. These results lead to conclude that at higher thicknesses, depletion charge densities dominate the final decision of phase transition temperature, whereas at lower thicknesses existence of dead layer dominates the final decision of phase transition temperature.

5.2 Future Work

As a future step to our study, different real life factors such as dislocation networks can be taken into account of the thin film capacitor system via incorporation of corresponding energy calculation into the LGD formalism. Thicker systems can be studied in order to show different nature of built-in field when the film thickness is higher than the depletion layer width of metal-semiconductor interface. Also, a completely different system would contain semiconducting electrodes such as RuO_2 (E_{gap}= 2.4 eV) instead of metallic ones, in that case a p–n junction would form at the electrode-film interface and screening

length of the polarization charges, i.e., dead layer thicknesses would be very different. Then time-dependant ferroelectric behaviour of films with different type of electrodes can be compared numerically to extract fatigue-related information which is experimentally discussed in some studies in literature [18].

APPENDIX 1

Finite difference discretization for potential calculation of the dead layer is

$$\frac{\phi(i,j+1)+\phi(i,j-1)-2\phi(i,j)}{dx^2}+\frac{\phi(i+1,j)+\phi(i-1,j)-2\phi(i,j)}{dz^2}=-\frac{\rho}{\varepsilon_r^d\varepsilon_0}$$

$$\frac{\phi(i,j+1)+\phi(i,j-1)+\phi(i+1,j)+\phi(i-1,j)-4\phi(i,j)}{dz^2}=-\frac{\rho}{\varepsilon_r^d\varepsilon_0} \quad \text{(A1.1)}$$

$$\phi(i,j)=\frac{dz^2\rho}{4\varepsilon_r^d\varepsilon_0}+\frac{\phi(i,j+1)+\phi(i,j-1)+\phi(i+1,j)+\phi(i-1,j)}{4}$$

For the ferroelectric layer, polarization is a separate component of displacement as shown in the Eq. (3.24). So, finite difference discretization for ferroelectric layer becomes

$$\frac{\phi(i,j+1)+\phi(i,j-1)-2\phi(i,j)}{dx^2}+\frac{\phi(i+1,j)+\phi(i-1,j)-2\phi(i,j)}{dz^2}=$$

$$\frac{1}{\varepsilon_b\varepsilon_0}\left(\frac{P_3(i+1,j)-P_3(i-1,j)}{2dz}+\frac{P_1(i,j+1)-P_1(i,j-1)}{2dx}-\rho\right)$$

$$\frac{\phi(i,j+1)+\phi(i,j-1)+\phi(i+1,j)+\phi(i-1,j)-4\phi(i,j)}{dz^2}=$$

$$\frac{1}{\varepsilon_b\varepsilon_0}\left(\frac{P_3(i+1,j)-P_3(i-1,j)+P_1(i,j+1)-P_1(i,j-1)}{2dz}-\rho\right) \quad \text{(A1.2)}$$

$$\phi(i,j)=\frac{dz^2}{4\varepsilon_b\varepsilon_0}\left(\rho-\frac{P_3(i+1,j)-P_3(i-1,j)+P_1(i,j+1)-P_1(i,j-1)}{2dz}\right)$$

$$+\frac{\phi(i,j+1)+\phi(i,j-1)+\phi(i+1,j)+\phi(i-1,j)}{4}$$

When the polarizations in two directions are coupled, any of them are treated as ferroelectric polarizations

$$G\left(\frac{\partial^2 P_1}{\partial x^2}+\frac{\partial^2 P_1}{\partial z^2}\right)=4\alpha_1^m P_1+4(2\alpha_{11}^m+\alpha_{12}^m)P_1^3+4\alpha_{13}^m P_1 P_3^2+6(2\alpha_{111}+2\alpha_{112})P_1^5$$

$$+4(2\alpha_{112}+\alpha_{123})P_1^3 P_3^2+4\alpha_{112}P_3^4 P_1-E_1 \quad \text{(A1.3)}$$

54

$$G\left(\frac{\partial^2 P_3}{\partial x^2} + \frac{\partial^2 P_3}{\partial z^2}\right) = 2\alpha_3^m P_3 + 4\alpha_{33}^m P_3^3 + 4\alpha_{13}^m P_1^2 P_3 + 6\alpha_{111} P_3^5$$

$$+2(2\alpha_{112} + \alpha_{123})P_1^4 P_3 + 8\alpha_{112} P_3^3 P_1^2 - E_3 \tag{A1.4}$$

Discretization of the above equations:

$$G\left(\frac{P_1(i+1,j) + P_1(i-1,j) - 2P_1(i,j)}{dz^2} + \frac{P_1(i,j+1) + P_1(i,j-1) - 2P_1(i,j)}{dx^2}\right) =$$

$$4\alpha_1^m P_1(i,j) + 4(2\alpha_{11}^m + \alpha_{12}^m)P_1^3(i,j) + 4\alpha_{13}^m P_1(i,j)P_3^2(i,j) + 6(2\alpha_{111} + 2\alpha_{112})P_1^5(i,j) \tag{A1.5}$$

$$+4(2\alpha_{112} + \alpha_{123})P_1^3(i,j)P_3^2(i,j) + 4\alpha_{112}P_3^4(i,j)P_1(i,j) - E_1(i,j)$$

$$G\left(\frac{P_3(i+1,j) + P_3(i-1,j) - 2P_3(i,j)}{dz^2} + \frac{P_3(i,j+1) + P_3(i,j-1) - 2P_3(i,j)}{dx^2}\right)$$

$$= 2\alpha_3^m P_3(i,j) + 4\alpha_{33}^m P_3^3(i,j) + 4\alpha_{13}^m P_1^2(i,j)P_3(i,j) + 6\alpha_{111}P_3^5(i,j) + \tag{A1.6}$$

$$2(2\alpha_{112} + \alpha_{123})P_1^4(i,j)P_3(i,j) + 8\alpha_{112}P_3^3(i,j)P_1^2(i,j) - E_3(i,j)$$

$$P_1(i,j)\left(\frac{-2G}{dz^2} + \frac{-2G}{dx^2}\right) = 4\alpha_1^m P_1(i,j) + 4(2\alpha_{11}^m + \alpha_{12}^m)P_1^3(i,j) + 4\alpha_{13}^m P_1(i,j)P_3^2(i,j) +$$

$$6(2\alpha_{111} + 2\alpha_{112})P_1^5(i,j) + 4(2\alpha_{112} + \alpha_{123})P_1^3(i,j)P_3^2(i,j) + 4\alpha_{112}P_3^4(i,j)E_1(i,j) - E_1(i,j) \tag{A1.7}$$

$$-G\left(\frac{P_1(i+1,j) + P_1(i-1,j)}{dz^2} + \frac{P_1(i,j+1) + P_1(i,j-1)}{dx^2}\right)$$

$$P_3(i,j)\left(\frac{-2G}{dz^2} + \frac{-2G}{dx^2}\right) = 2\alpha_3^m P_3(i,j) + 4\alpha_{33}^m P_3^3(i,j) + 4\alpha_{13}^m P_1^2(i,j)P_3(i,j) + 6\alpha_{111}P_3^5(i,j)$$

$$+2(2\alpha_{112} + \alpha_{123})P_1^4(i,j)P_3(i,j) + 8\alpha_{112}P_3^3(i,j)P_1^2(i,j) - E_3(i,j) \tag{A1.8}$$

$$-G\left(\frac{P_3(i+1,j) + P_3(i-1,j)}{dz^2} + \frac{P_3(i,j+1) + P_3(i,j-1)}{dx^2}\right)$$

When dx=dz;

$$P_1(i,j)\left(\frac{-4G}{dz^2}\right) = 4\alpha_1^m P_1(i,j) + 4(2\alpha_{11}^m + \alpha_{12}^m)P_1^3(i,j) + 4\alpha_{13}^m P_1(i,j)P_3^2(i,j) +$$

$$6(2\alpha_{111} + 2\alpha_{112})P_1^5(i,j) + 4(2\alpha_{112} + \alpha_{123})P_1^3(i,j)P_3^2(i,j) + 4\alpha_{112}P_3^4(i,j)P_1(i,j) \tag{A1.9}$$

$$-E_x(i,j) - G\left(\frac{P_1(i+1,j) + P_1(i-1,j) + P_1(i,j+1) + P_1(i,j-1)}{dz^2}\right)$$

$$P_1(i,j) = \frac{-dz^2}{G}[\alpha_1^m P_1(i,j) + (2\alpha_{11}^m + \alpha_{12}^m)P_1^3(i,j) + \alpha_{13}^m P_1(i,j)P_3^2(i,j) +$$

$$1.5(2\alpha_{111} + 2\alpha_{112})P_1^5(i,j) + (2\alpha_{112} + \alpha_{123})P_1^3(i,j)P_3^2(i,j) + \alpha_{112}P_4^4(i,j)P_1(i,j)] \quad \text{(A1.10)}$$

$$+ \frac{dz^2}{4G}E_1(i,j) + \frac{P_1(i+1,j) + P_1(i-1,j) + P_1(i,j+1) + P_1(i,j-1)}{4}$$

$$P_3(i,j)\left(\frac{-4G}{dz^2}\right) = 2\alpha_3^m P_3(i,j) + 4\alpha_{33}^m P_3^3(i,j) + 4\alpha_{13}^m P_1^2(i,j)P_3(i,j) +$$

$$6\alpha_{111}P_3^5(i,j) + 2(2\alpha_{112} + \alpha_{123})P_1^4(i,j)P_3(i,j) + 8\alpha_{112}P_3^3(i,j)P_1^2(i,j) \quad \text{(A1.11)}$$

$$-E_3(i,j) - G\left(\frac{P_3(i+1,j) + P_3(i-1,j) + P_3(i,j+1) + P_3(i,j-1)}{dz^2}\right)$$

$$P_3(i,j) = \frac{-dz^2}{G}[0.5\alpha_3^m P_3(i,j) + \alpha_{33}^m P_3^3(i,j) + \alpha_{13}^m P_1^2(i,j)P_3(i,j) +$$

$$1.5\alpha_{111}P_3^5(i,j) + 0.5(2\alpha_{112} + \alpha_{123})P_1^4(i,j)P_3(i,j) + 2\alpha_{112}P_3^3(i,j)P_1^2(i,j)] + \quad \text{(A1.12)}$$

$$\frac{dz^2}{4G}E_3(i,j) + \frac{P_3(i+1,j) + P_3(i-1,j) + P_3(i,j+1) + P_3(i,j-1)}{4}$$

Modified dielectric stiffness coefficients are retrieved from [34] as the following:

$$\alpha_1^m = \alpha_1 - u_m\frac{Q_{11} + Q_{12}}{S_{11} + S_{12}}, \quad \alpha_3^m = \alpha_1 - u_m\frac{2Q_{12}}{S_{11} + S_{12}}$$

$$\alpha_{11}^m = \alpha_{11} + \frac{1}{2}\frac{1}{S_{11}^2 - S_{12}^2}\left[(Q_{11}^2 + Q_{12}^2)S_{11} - 2Q_{11}Q_{12}S_{12}\right], \alpha_{33}^m = \alpha_{11} + \frac{Q_{12}^2}{S_{11} + S_{12}} \quad \text{(A1.13)}$$

$$\alpha_{12}^m = \alpha_{12} - \frac{1}{S_{11}^2 - S_{12}^2}\left[(Q_{11}^2 + Q_{12}^2)S_{12} - 2Q_{11}Q_{12}S_{11}\right] + \frac{Q_{44}^2}{2S_{44}}, \alpha_{13}^m = \alpha_{12} + \frac{Q_{12}(Q_{11} + Q_{12})}{S_{11} + S_{12}}$$

Dielectric stiffness and electrostrictive coefficients and elastic stiffness constants for BaTiO$_3$ are as follows:

Table A.1. The dielectric stiffnesses, electrostrictive coefficients, elastic constants and other constants of $BaTiO_3$ used in numerical calculations

Constant	Value
Curie Point (˚C)	130
C (Curie Constant)	1.5×10^5
α_1 (m/F)	$3.3(T-130) \times 10^5$
α_{11} (m^5/C^2F)	-6.381×10^8
α_{111} (m^5/C^2F)	6.6×10^9
α_{12} (m^5/C^2F)	-0.0345×10^8
α_{112} (m^9/C^4F)	18.14×10^8
α_{123} (m^9/C^4F)	-7.545×10^9
Q_{11} (m^4/C^2)	0.11
Q_{12} (m^4/C^2)	-0.043
Q_{44} (m^4/C^2)	5.165×10^{-12}
S_{11} (m^2/N)	8.3×10^{-12}
S_{12} (m^2/N)	-2.7×10^{-12}
S_{44} (m^2/N)	9.24×10^{-12}
u_m (misfit strain)	-0.0169
G (m^4N/C^{-2})	3×10^{-10}

.

APPENDIX 2

The system analyzed in [37] is already given in Figure 3.1. The analytical approach in [37] is based on finding the point of loss of stability of the paraelectric phase for a ferroelectric slab with dead layers. While the system in [37] is treated in one half of the film with dead layers and the film being very thick compared to the dead layers, this approach was generalized in [38] and this general approach is followed by full treatment of the film with high-*k* dead layers. Going back to the system in Figure 3.1, for a given dead layer (1 BaTiO$_3$ unit cell thick, ~0.4 nm, in this thesis) and film thickness, *d* and *L* respectively, the boundary conditions of the system can be written as

$$D_3^F - D_3^d = 0 \quad @z = \pm L/2, \tag{A2.1}$$

$$\phi_F = \phi_d \quad @z = \pm L/2 \tag{A2.2a}$$

$$\phi_d = 0 \quad @z = L/2 + d \tag{A2.2b}$$

$$\phi_d = 0 \quad @z = -L/2 - d \tag{A2.2c}$$

where $D_3^F = \varepsilon_0\varepsilon_b E_3^F + P$ and $D_3^d = \varepsilon_0\varepsilon_r^d E_3^d$ are the dielectric displacements while $\phi_{F,d}$ are the potentials in the FE and the dead layer respectively. *L* is the FE film thickness (See Figure 3.1). From Eqn. A2.1, one gets

$$-\varepsilon_0\varepsilon_b \frac{\partial \phi_F}{\partial z} + P_3 + \varepsilon_0\varepsilon_r^d \frac{\partial \phi_d}{\partial z} = 0 \quad @z = \pm L/2. \tag{A2.3}$$

In the absence of free charges $\nabla D = 0$ both in the FE and the dead layers. Writing these conditions in terms of the potential and polarization in the FE film, we get

$$\frac{\partial^2 \varphi_F}{\partial z^2} + \varepsilon_\perp \frac{\partial^2 \varphi_F}{\partial x^2} = \frac{1}{\varepsilon_0} \frac{\partial P_3}{\partial z}, \tag{A2.4}$$

where $\varepsilon_\perp$ is the dielectric constant of the FE along the *x-y* plane of the film (Calculated as

approximately 40 from the simulations and this value is used) and

$$\varepsilon_0 \left(\varepsilon_r^d \frac{\partial^2 \phi_d}{\partial z^2} + \varepsilon_\perp^d \frac{\partial^2 \phi_d}{\partial x^2} \right) = 0 \tag{A2.5}$$

for the dead layer. For convenience, it is assumed that the dead layer is isotropic and $\varepsilon_r^d = \varepsilon_\perp^d$ with $\varepsilon_\perp^d$ being the dielectric constant of the dead layer along the film plane. The linear equation of state of the FE that is obtained by minimization of the Landau-Ginzburg free energy with its lowest order terms is:

$$AP_3 - G\frac{\partial^2 P_3}{\partial x^2} = -\frac{\partial \phi_F}{dz} \tag{A2.6}$$

where the gradient of P_3 along z has been neglected, $A = (T - T_C)/\varepsilon_0 C + M$ where T is temperature, T_C is the transition temperature in bulk form, C is the Curie constant, M represents any contribution of strain in the case of a FE on a substrate [39] (See the modified coefficient of the lowest order term in P in the free energy in [34]), G is the gradient energy coefficient. Note that the energy due to gradients along z is much less than the gradients of P_3 along x, allowing one to safely neglect gradients along z. To solve the polarization and the potential using the differential equations above together with the equation of state in the FE, one can use the Fourier transform to express the polarization and the potentials in the layers in terms of harmonics:

$$P_3 = \sum_k P_k e^{ikx}, \; \phi_F = \sum_k \phi_F^k e^{ikx}, \; \phi_d = \sum_k \phi_d^k e^{ikx} \tag{A2.7}$$

where P_k, ϕ_F^k and ϕ_d^k are the z-amplitudes of each harmonic in k. Inserting these Fourier transforms for a given k into Eqn.s A2.4, A2.5 and A2.6, we get:

$$\frac{d^2\phi_F^k}{dz^2} + q^2\phi_F^k = 0 \tag{A2.8}$$

$$\frac{d^2\phi_d^k}{dz^2} - k^2\phi_d^k = 0 \tag{A2.9}$$

59

where $q = (\varepsilon_\perp k^2 / |\varepsilon_k|)^{1/2}$ and $\varepsilon_k = \left(\dfrac{1}{\varepsilon_0(A + Gk^2)} + \varepsilon_b \right)$. The value of k that corresponds to

the wave vector of the polarization at the transition temperature has to be found, which will

be explained at the end of this Appendix. The solutions of Eq.A2.8 and A2.9 that satisfy the

boundary conditions given in Eq. A2.1 and A2.2 are:

$$\varphi_F^k = A \cos qz + B \sin qz \qquad (A2.10)$$

$$\phi_d^k = C \sinh k(z - (L/2 + d)) + D \cosh k(z - (L/2 + d)) \qquad (A2.11)$$

where A, B, C and the D are the amplitudes in the general solution and

$$q = (\varepsilon_\perp k^2 / |\varepsilon_k|)^{1/2} \qquad (A2.12)$$

Using the BCs given in Eq. A2.1 and A2.2, we get two equations with two unknowns,

B and C from Eqn.s A2.10 and A2.11:

$$B \left[q \cos \frac{qL}{2} + \frac{q}{\varepsilon_0(A + Gk^2)} \cos \frac{qL}{2} \right] - \varepsilon_r^d kC \cosh - \frac{kL}{2} = 0 \qquad (A2.13a)$$

$$B \sin \frac{qL}{2} - C \sinh - \frac{kL}{2} = 0 \qquad (A2.13b)$$

For a non-trivial solution to exist, the determinants of the coefficients in Eqn.s

A2.13a and A2.13b has to be zero, giving us,

$$B \left[\sinh \frac{kL}{2} \left(q \cos \frac{qL}{2} + \frac{q}{\varepsilon_0(A + Gk^2)} \cos \frac{qL}{2} \right) + \varepsilon_r^d k \cosh - \frac{kL}{2} \sin \frac{qL}{2} \right] = 0 \qquad (A2.14)$$

meaning that

$$\sinh \frac{kL}{2} \left(q \cos \frac{qL}{2} + \frac{q}{\varepsilon_0(A + Gk^2)} \cos \frac{qL}{2} \right) + \varepsilon_r^d k \cosh - \frac{kL}{2} \sin \frac{qL}{2} = 0 \qquad (A2.15)$$

After some algebra on Eqn. A2.15, one gets

$$\tan \frac{qL}{2} = \frac{\sqrt{|\varepsilon_k| \varepsilon_\perp}}{\varepsilon_r^d} \tanh \frac{kd}{2} \qquad (A2.16a)$$

where

$$|\varepsilon_k| = \left(\frac{1}{\varepsilon_0(A + gk^2)} + \varepsilon_b \right)$$ (A2.16b)

which was previously obtained by the authors of [37] through a similar route. Their approach is somewhat repeated here for tractability of results in this thesis. Eqn. A16a is solved using a numerical approach and the k value that yields the highest transition temperature from the paraelectric state into the ferroelectric state for a given d (1 unit cell thick) is sought. The calculations in the single domain state regime which correspond to thicknesses smaller than 3 nm are not carried out and is outside the scope of our analysis. Also note that the described method is applied for the validation of the simulation results and do not reflect any depletion charge related effects, which are separately given only by the numerical simulation presented in this thesis.

REFERENCES

1. Cohen, R.E., *Origin of ferroelectricity in perovskite oxides.* Nature, 1992. **358**: p. 136-138.

2. M. B. Smith, K.P., T. Siegrist, P. L. Redmond, E. C. Walter, R. Seshadri, L. E. Brus, M. L. Steigerwald, *Crystal Structure and the Paraelectric-to-Ferroelectric Phase Transition of Nanoscale BaTiO3.* J. of Am. Chem. Soc., 2008. **130**: p. 6955–6963.

3. Safari, A., R.K. Panda, and V.F. Janas, *Ferroelectricity: Materials, characteristics & applications*, in *Advanced Ceramic Materials: Applications of Advanced Materials in a High-Tech Society I*, H. Mostaghaci, Editor 1996, Trans Tech Publications Ltd: Stafa-Zurich. p. 35-69.

4. Merz, W.J., *Double Hysteresis Loop of BaTiO3 at the Curie Point.* Physical Review, 1953. **91**(3): p. 513.

5. Damjanovic, D., *Ferroelectric, dielectric and piezoelectric properties of ferroelectric thin films and ceramics.* Reports on Progress in Physics, 1998. **61**(9): p. 1267-1324.

6. Tagantsev, A.K. and G. Gerra, *Interface-induced phenomena in polarization response of ferroelectric thin films.* Journal of Applied Physics, 2006. **100**(5): p. 051607-051607-28.

7. Ravez, J., *Ferroelectricity in solid state chemistry.* Comptes Rendus de l'Académie des Sciences - Series IIC - Chemistry, 2000. **3**(4): p. 267-283.

8. Shaw, T.M., S. Trolier-McKinstry, and P.C. McIntyre, *The properties of ferroelectric films at small dimensions.* Annual Review of Materials Science, 2000. **30**: p. 263-298.

9. Arredondo, M., et al., *Structural defects and local chemistry across ferroelectric-electrode interfaces in epitaxial heterostructures.* Journal of Materials Science, 2009. **44**(19): p. 5297-5306.

10. Hideharu, M., *Calculation of band bending in ferroelectric semiconductor.* New Journal of Physics, 2000. **2**(1): p. 8.

11. Blom, P.W.M., et al., *FERROELECTRIC SCHOTTKY DIODE.* Physical Review Letters, 1994. **73**(15): p. 2107-2110.

12.   Lüth, H., *Surfaces and interfaces of solid materials*1995: Springer.

13.   Kolasinski, K.W., *Surface Science: Foundations of Catalysis and Nanoscience*2008: Jonh Wiley & Sons.

14.   Bube, R.H., *Electrons in Solids: an introductory survey*. 3rd edition ed1992, San Diego, CA: Academic Press Inc.

15.   Zeghbroeck, B.V., *Metal-Semiconductor Contacts*, in *Principles of Semiconductor Devices*2007.

16.   Bratkovsky, A.M. and A.P. Levanyuk, *Domains in ultrathin ferroelectric films with metallic and semiconducting electrodes*. Ferroelectrics, 2007. **359**: p. 1-+.

17.   Suo, Z., *Stress and strain in ferroelectrics*. Current Opinion in Solid State & Materials Sceince, 1998. **3**: p. 486-489.

18.   Jin, H.Z. and J. Zhu, *Size effect and fatigue mechanism in ferroelectric thin films*. Journal of Applied Physics, 2002. **92**(8): p. 4594-4598.

19.   Matthews, J.W. and A.E. Blakeslee, *Defects in epitaxial multilayers: I. Misfit dislocations*. Journal of Crystal Growth, 1974. **27**: p. 118-125.

20.   Chu, M.W., et al., *Impact of misfit dislocations on the polarization instability of epitaxial nanostructured ferroelectric perovskites*. Nature Materials, 2004. **3**(2): p. 87-90.

21.   Nagarajan, V., et al., *Misfit dislocations in nanoscale ferroelectric heterostructures*. Applied Physics Letters, 2005. **86**(19).

22.   Zhang, Y., J. Li, and D. Fang, *Oxygen-vacancy-induced memory effect and large recoverable strain in a barium titanate single crystal*. Physical Review B, 2010. **82**(6): p. 064103.

23.   Aggarwal, S. and R. Ramesh, *Point defect chemistry of metal oxide heterostructures*. Annual Review of Materials Science, 1998. **28**: p. 463-499.

24.   Folkman, C.M., et al., *Study of defect-dipoles in an epitaxial ferroelectric thin film*. Applied Physics Letters, 2010. **96**(5): p. 052903.

25.   Pintilie, L. and M. Alexe, *Metal-ferroelectric-metal heterostructures with Schottky contacts. I. Influence of the ferroelectric properties*. Journal of Applied Physics,

2005. **98**(12).

26.   Pintilie, L., et al., *Metal-ferroelectric-metal structures with Schottky contacts. II. Analysis of the experimental current-voltage and capacitance-voltage characteristics of Pb(Zr,Ti)O-3 thin films.* Journal of Applied Physics, 2005. **98**(12).

27.   Glinchuk, M.D., B.Y. Zaulychny, and V.A. Stephanovich, *Depolarization field in thin ferroelectric films with account of semiconductor electrodes.* Ferroelectrics, 2005. **316**: p. 1-6.

28.   Misirlioglu, I.B., M.B. Okatan, and S.P. Alpay, *Asymmetric hysteresis loops and smearing of the dielectric anomaly at the transition temperature due to space charges in ferroelectric thin films.* Journal of Applied Physics, 2010. **108**(3): p. 034105.

29.   Bratkovsky, A.M. and A.P. Levanyuk, *Ferroelectric phase transitions in films with depletion charge.* Physical Review B, 2000. **61**(22): p. 15042.

30.   Falk, F., *LANDAU THEORY AND MARTENSITIC PHASE-TRANSITIONS.* Journal De Physique, 1982. **43**(NC-4): p. 3-15.

31.   Lev Davidovic Landau, E.M.L., Lev Petrovich Pitaevskii, *Electrodynamics of Continuous Media.* 2 ed. Course of Theoretical Physics. Vol. 8. 1982, Oxford: Elsevier Butterworth-Heinemann. 476.

32.   Glinchuk, M.D., E.A. Eliseev, and A.N. Morozovska, *Influence of built-in internal electric field on ferroelectric film properties and phase diagram.* Ferroelectrics, 2007. **354**: p. 86-98.

33.   Marvan, M. and J. Fousek, *Electrostatic Energy of Ferroelectrics with Nonhomogeneous Distributions of Polarization and Free Charges.* physica status solidi (b), 1998. **208**(2): p. 523-531.

34.   Pertsev, N.A., A.G. Zembilgotov, and A.K. Tagantsev, *Effect of mechanical boundary conditions on phase diagrams of epitaxial ferroelectric thin films.* Physical Review Letters, 1998. **80**(9): p. 1988-1991.

35.   Hong, L. and et al., *Influence of size-dependent electrostatic energy on the ferroelectric nanodot domain structure by phase field method.* Journal of Physics D: Applied Physics, 2009. **42**(12): p. 122005.

36.   Gil, S., M.E. Saleta, and D. Tobia, *Experimental study of the Neumann and Dirichlet boundary conditions in two-dimensional electrostatic problems.* American

Journal of Physics, 2002. **70**(12): p. 1208-1213.

37.   Chensky, E.V. and V.V. Tarasenko, *THEORY OF PHASE-TRANSITIONS TO INHOMOGENEOUS STATES IN FINITE FERROELECTRICS IN AN EXTERNAL ELECTRIC-FIELD.* Zhurnal Eksperimentalnoi I Teoreticheskoi Fiziki, 1982. **83**(3): p. 1089-1099.

38.   Sidorkin, A.S., *Domain Structure in Ferroelectrics and Related Materials*2006: Cambridge International Science Publishing.

39.   Chang, L.W., M. McMillen, and J.M. Gregg, *The influence of point defects and inhomogeneous strain on the functional behavior of thin film ferroelectrics.* Applied Physics Letters, 2009. **94**(21).